COMPUTATION OF DYNAMICAL STRUCTURES FOR DYNAMICAL BILLIARDS AND PARAMETER DRIFT EQUATIONS

by

Patrick Bishop
A Dissertation
Submitted to the
Graduate Faculty
of
George Mason University
In Partial fulfillment of
The Requirements for the Degree
of
Doctor of Philosophy
Mathematics

Committee:

______________________	Dr. Evelyn Sander, Dissertation Director
______________________	Dr. Thomas Wanner, Committee Member
______________________	Dr. Tyrus Berry, Committee Member
______________________	Dr. Anne Costolanski, Committee Member
______________________	Dr. Maria Emelianenko, Department Head
______________________	Dr. Gerald L. R. Weatherspoon, Associate Dean for Undergraduate and Graduate Affairs, College of Science
______________________	Dr. Cody Edwards, Interim Dean, College of Science
Date: ______________________	Fall 2024 George Mason University Fairfax, VA

Computation of Dynamical Structures for Dynamical Billiards and Parameter Drift Equations

A dissertation submitted in partial fulfillment of the requirements for the degree of Doctor of Philosophy at George Mason University

By

Patrick Bishop
Bachelor of Science
George Mason University, 2015

Director: Dr. Evelyn Sander, Professor
Department of Department of Mathematics

Fall 2024
George Mason University
Fairfax, VA

Dedication

People warn you about how much you will have to sacrifice to earn a Ph.D but, they often fail to warn you about what will have to be sacrificed by those you share a life with. Thank you Jordy Liberto for being a constant source of love and support throughout this process. I could not have achieved this goal without you.

Acknowledgments

I would like to thank the following people who made this possible: Evelyn Sander, Thomas Wanner, Tyrus Berry, Anne Costolanski, Jason Mireles-James, and all the other supportive faculty of the Math department at GMU who provided me with many opportunities. I would especially like to thank my parents Vicki Bishop and Bill Bishop for always pushing me to be better even when I was at my worst, Jordy Liberto for always challenging me to grow, and Drisana Sutch for being the best roommate a guy could ask for. Lastly, I would like to thank all my close friends and family that have not been named personally. I have too many to name here but you each know who you are and that I am grateful for your support. Aristotle was attributed to saying "he who has many friends, has no friends." I have never known this to be true so I suppose he must have not been well liked.

Table of Contents

List of Tables

List of Figures

Abstract

COMPUTATION OF DYNAMICAL STRUCTURES FOR DYNAMICAL BILLIARDS AND PARAMETER DRIFT EQUATIONS

Patrick Bishop, PhD

George Mason University, 2024

Dissertation Director: Dr. Evelyn Sander

In this thesis, we will be looking at computational methods for studying area preserving maps. We will demonstrate a new computational method for computing billiard maps, apply existing methods such as the weighted Birkhoff average (WBA) to the billiards system, and construct a way to compute the stable and unstable manifolds by way of the parametrization method. Other methods have been used to compute the billiard map for convex tables but we have constructed a new method that is analytic and can work implicitly with the parametrized form of the ellipse. The parametrized form for the ellipse allows one to easily perturb the ellipse in a way that mimics the Fourier series which becomes more useful with the parametrization method. Previously, WBA and the parametrization method have been used on explicit systems but we will develop a novel method of applying them to an implicit form for the billiard map. This research is related to the Birkhoff conjecture since our focus will be on billiard tables that are perturbations of the ellipse. In the second part of this thesis, we will focus on applying the method of weighted Birkhoff averages to parameter drift problems to study the breakup of tori. In particular, we will look at the periodically forced Duffing oscillator and show how using the method of weighted Birkhoff averages speeds up this process and allows for quicker measurements of break up probabilities.

Chapter 1: Introduction to Billiards

1.1 Introduction

Billiards has been a beloved game since the 14th century. It also provides a rich mathematical playground which mathematicians have been studying since Birkhoff first discussed the 2-D billiard system with convex boundaries in [1]. It is a system comprised of a two dimensional domain with a point bouncing elastically within the domain. The famous Birkhoff conjecture, which we will discuss in more detail in section 1.3, has been the subject of interest since being first proposed. In short, the Birkhoff conjecture states that the only smooth totally integrable billiard systems are ellipses. Since this conjecture was first proposed, research has been aimed at proving this conjecture in a few different ways. Some have focused on the perturbed ellipse case as in [2] while others have proved local versions of the conjecture as in [3, 4]. In 2023, Baracco and Bernardi proved that a totally integrable strictly-convex symplectic billiard table, whose boundary has strictly positive curvature, must be an ellipse, [5]. For more discussion on open problems in Birkhoff billiards, refer to [6].

Chaos in billiards systems has also been an interest of research ever since Bunimovich showed there existed tables with only focusing components (focusing trajectories like a lens) that contained chaotic orbits, [7,8]. An introduction to chaotic billiards can be found in [9]. Further research into systems with chaos can be found in [10,11]. Research in billiards has been extended to many physical models including studying dynamics in nuclear billiards [12], and celestial mechanics, where the billiard system is subject to the force of gravity [13,14]. Other research has been focused on billiard tables subject to a magnetic field such as in [15].

We now describe our work on billiards. This research is joint with Jason Mireles James and Evelyn Sander.We will discuss several ways to identify aspects of the phase space for the billiard map. This will be discussed more thoroughly in section 1.6. To distinguish chaotic orbits from regular orbits we will use the weighted Birkhoff average, which is a method of computing Birkhoff averages of an orbit. This numerical method converges slowly when the orbit is chaotic and quickly when the orbit is non-chaotic, thereby allowing us to distinguish between orbit types. To study non-chaotic orbits, we will use the rotation number, a Birkhoff average which computes the average amount that the ball moves about the ellipse on each bounce.

We will be focused on continuously differentiable boundaries, in particular, of the perturbed ellipse since we are interested in applications to the Birkhoff conjecture. Although there are many methods for computing billiards, we have found that previous methods are not sufficient for our goals. This is in part due to numerical difficulties which we will outline later in section 1.4. Additionally, our method allowed us more freedom in how we describe the perturbed ellipse. For example, Figure 1.1 shows orbits for an ellipse and a perturbed ellipse. Finally, we are interested in computing the stable and unstable manifolds using the parametrization method, and our representation for the ellipse allows us to set up the tools needed. To this end, we construct the billiard map as an implicitly defined analytic system, since that is most efficient and accurate for computing the stable and unstable manifold via the parametrization method.

This chapter has the following structure. In section 1.2, we describe the Birkhoff billiards map, and give general theoretical results. In section 1.3, we will discuss the billiard map and properties of some elementary tables such as the circle and the ellipse. In section 1.4, we give an overview of other numerical methods that have been implemented to simulate billiard systems for various tables shapes, including convex and non-convex tables. In section 1.5, we describe our approach to simulating orbits of the billiard system for the perturbed ellipse case. This method works for tables that have smooth boundaries and are convex. In section 1.6, we show some results from our simulations as well as describe the methods

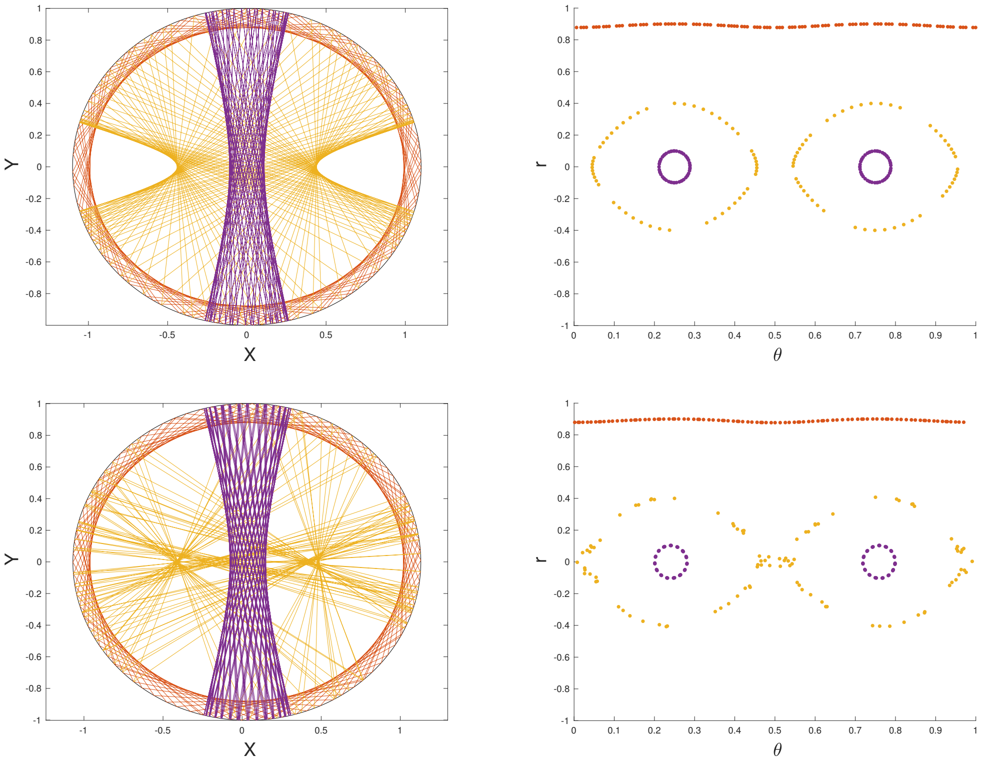

Figure 1.1: The formulation for the billiard map is determined completely by the points of contact on the boundary and the direction of the balls path. The physical tables (left column) versus the phase space (right column) where r and θ are defined by definition 1.2.3 for three trajectories in the billiard map on the ellipse with coefficients $a_1 = 1.1$ and $b_1 = 1$ (top row) from equation (1.6) and the perturbed ellipse with $a_1 = 1.1, a_2 = 0.03$ and $b_1 = 1, b_2 = 0.03$ (bottom row) from equation (1.10). Three orbits were taken starting from $\theta = 0.25$ each having an orbit length of 100.

used to analyze the phase space for the perturbed ellipse table including rotation number and the weighted Birkhoff average. We also discuss a method for finding periodic orbits using the method of multiple shooting. In section 1.5.2, we describe how to reformulate this method as an analytic system and extend it into the complex phase space. This method is not effective for iteration, but it is effective for continuation, allowing us to continue real solutions into the complex phase space. This allows us to compute a Fourier series for the parametrization method, which leads to an effective way to approximate the Taylor series with a polynomial. We use this Taylor series approximation to calculate the stable and unstable manifolds for periodic orbits.

1.2 Dynamical Billiards

Dynamical billiards, as developed by Birkhoff, is an iterated map on a phase space. Birkhoff adapted this physical game to a dynamical systems model as a way to simplify gas dynamics. The billiard system consists of a 2-D domain $\mathcal{D}$ and a point particle (radius zero) moving along straight line paths within $\mathcal{D}$ until it hits the boundary, at which point it is reflected elastically. More formally, billiard tables are defined as found in [9]:

Definition 1.2.1. *A billiard table $\mathcal{D}$ is the closure of a bounded open connected domain $\mathcal{D} \subset \mathbb{R}^2$ such that $\partial\mathcal{D}$ satisfies the following:*

1. *The boundary Γ is a finite union of smooth compact curves.*
2. *The boundary components Γ_i can intersect each other only at their endpoints.*

Now that we have the definition of the table, we can define more generally the billiard system.

Definition 1.2.2. *A billiard system consists of a point particle and a domain $\mathcal{D}$ where the point particle moves in straight lines within the domain $\mathcal{D}$ according to the following criteria. Let $v(t) \in \mathbb{R}^2$ for $t \in [0, \infty)$ denote the trajectory of the particle within the billiard table $\mathcal{D}$. Let $v(0) \in \Gamma$ denote the starting point of the ball on the boundary. Furthermore,*

1. *$v(t)$ consists of continuous line segments each of which is twice differentiable with respect to t.*

2. *$v(t)$ moves within $\mathcal{D}$ along straight lines until it reaches the boundary for some $t^* > 0$ at which point it is reflected elastically back into $\mathcal{D}$ according to the law of reflection.*

In this treatment, we restrict the domain to those with convex and smooth boundaries as done in [16]. We denote the boundary of $\mathcal{D}$ with Γ which will be assumed to be a continuously differentiable curve, parametrized by B where $B(\theta) = (x(\theta), y(\theta))$ such that:

$$B : [0, 1] \to \mathbb{R}^2$$

with $B(0) = B(1)$ and $B([0, 1]) = \Gamma$. We also require B to have a counter-clockwise orientation on Γ and assume $B'(\theta)$ is well defined and non-zero for all θ. We assume that the curve does not intersect with itself at any point, that it is convex, and that the billiard ball moves with constant speed.

We now state the law of reflection.

Theorem 1.2.1. *Let $v, \hat{v}$ intersect on Γ, and assume v reflects to $\hat{v}$ at the point of intersection. Let n_p be the unit inward normal at the point of intersection on Γ. Then,*

$$\hat{v} = v - 2 \langle v, n_p \rangle n_p.$$

Proof. Figure 1.2 gives the geometric description for how this proof is structured. For any vector v we can find its orthogonal decomposition in the following way:

$$v = v_T + v_N \tag{1.1}$$

where v_T is the component parallel to the tangent line at the point of contact and v_N is the component orthogonal to the tangent line at point of contact. By the law of reflection, $\theta_1 = \theta_2$ where θ_1 is the angle made with the vector v and the normal vector at the point of

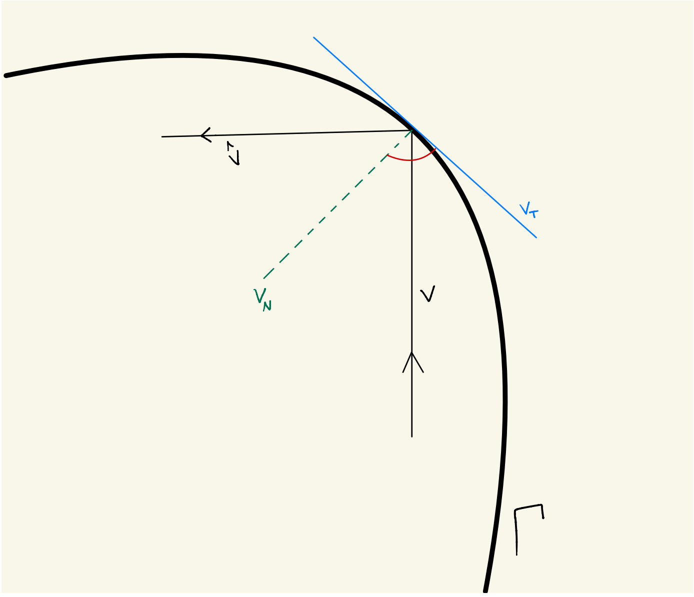

Figure 1.2: Reflection of a billiard ball off the boundary. The normal vector is the dotted green line, and the tangent vector is the blue line.

contact and θ_2 is the angle made with the vector $\hat{v}$ and the normal vector at the point of contact. Therefore, we can assume:

$$\hat{v} = v_T - v_N. \tag{1.2}$$

Then,

$$v - \hat{v} = (v_T + v_N) - (v_T - v_N) = 2v_N = 2\langle v, n_p \rangle n_p$$

where in the final line we substitute the expression for v_N with the expression for the projection of v onto n_p which by construction, is equal to v_N. Thus,

$$\hat{v} = v - 2\langle v, n_p \rangle n_p$$

$\square$

It is worth noting the following property of the convex table for the physical system. First discussed in [1], finding the next point of contact for the ball in a convex billiard system can be formulated as a minimization property. The minimization method can be stated with the following lemma.

Lemma 1.2.1 (Minimization Property). *Let x, y, and z be points on the boundary ellipse, $\mathcal{D}$. Suppose the line segment xy is reflected to the line yz at the point y. Then the angles made between the lines xy and yz with the tangent line at the point y are equal if and only if y is a critical point for the function:*

$$f(y) = |xy| + |yz|$$

where $|xy|$ and $|yz|$ are the 2-norm of each vector.

A proof for this lemma can be found in Levi and Tabachnikov [17] and relies on the Lagrange multiplier principle.

Since we know that trajectories move along straight lines between boundary collisions, the trajectory of the billiard is fully determined by the location of the boundary collision, along with the direction of the incoming vector v. This leads to an iterated map f, describing the ball's location. That is, the billiard ball will move along a straight path in the direction of v, where it will then intersect the boundary at a new point $B(\hat{\theta})$. Define γ to be the angle that v makes with the tangent vector at the point of contact and let $r = \cos\gamma$, at which point, the ball will then be reflected back according to theorem 1.2.1. Denote the new direction as $\hat{v}$, with angle $\hat{\gamma}$ and $\hat{r} = \cos\hat{\gamma}$. A geometric picture for this description can be found in figure 1.3. By theorem 1.2.1, the angle between v and the normal vector v_N, at $B(\hat{\theta})$ is equal to the angle between $\hat{v}$ and v_N at $B(\hat{\theta})$. This immediately implies that the angle between the tangent vector at the point of contact and v is equal to the angle between the tangent vector and $\hat{v}$. We formulate this in the following definition.

Definition 1.2.3. *Let $\mathcal{D}$ be a convex domain as in definition 1.2.1 with boundary Γ defined by a continuous parametrized curve, B. Let f be the map between successive collisions of a ball with the boundary. The phase space for this system is given by $I = \{(r, \theta) : -1 < r <$*

$1,\ 0 \le \theta < 1\}$ *where* r *represents the cosine of the angle* γ*, that the direction of the particle,* v *makes with the tangent of the boundary at the point* $B(\theta)$*. Let* $\hat{\theta}$ *be the parameter value corresponding to the point of next contact with the boundary. and let* $\hat{\gamma}$ *be the angle made with the trajectory of the ball after the collision with the boundary and the tangent line at* $B(\hat{\theta})$*, and let* $\hat{r} = \cos\hat{\gamma}$*. Then the billiard map is:*

$$(\hat{r}, \hat{\theta}) = f(r, \theta).$$

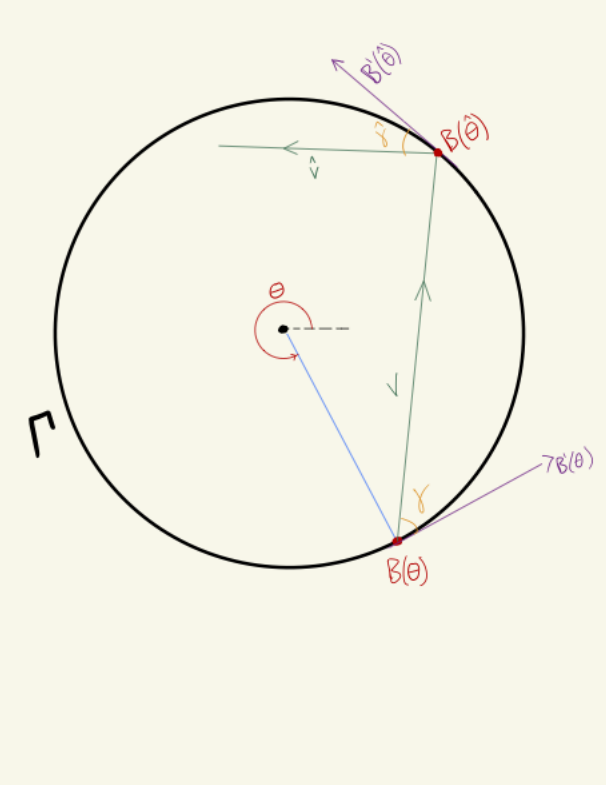

Figure 1.3: A point moving from the boundary at $B(\theta)$ with direction v to $B(\hat{\theta})$ with new direction $\hat{v}$.

We can construct a sequence of points $\{(r_k, \theta_k)\}$ with $(r_k, \theta_k) = f(r_{k-1}, \theta_{k-1})$. This sequence fully determines the billiard ball's trajectory within $\mathcal{D}$. In the above definition, we restrict $r \in (-1, 1)$ since at the endpoints of this interval, any r outside this range would be parallel to the tangent vector or pointing outside the table. Since we are restricting to convex tables, r would be pointing outside of the table. The phase space is a topological cylinder, since $B(0) = B(1)$. Often, the boundary is parametrized by arc length

$$s(t) = \int_0^t \sqrt{x'(k)^2 + y'(k)^2}dk,$$

where $\tilde{B}(t) = (x(t), y(t))$, but we have not chosen to do so. When parametrized by arclength,

$$\tilde{B} : [0, L] \to \mathbb{R}^2,$$

where L is the total length of the boundary which could be computed from our original parametrization via

$$L = \int_0^1 \sqrt{x'(t)^2 + y'(t)^2}dt.$$

The following are properties of the billiard map parametrized by arc length. The billiard map is an exact symplectic twist map with symplectic form $\cos \gamma ds$. This means that it preserves the area form. In simpler terms, this means that for the mapping $(x, y) \mapsto (\hat{x}, \hat{y})$, we can recover the information on $(y, \hat{y})$ just from knowing $(x, \hat{x})$. This is encoded by a generating function. Further discussion of billiards as a twist map and the generating function for the billiards system can be found in Meiss, [18, 19], and Himmelstrand [16] as well as in Golé [20]. A discussion on symplectic maps and their relation to Hamiltonian systems can be found in [21].

We define a symplectic map in the same way Golé does in [20] but using our billiard system notation:

Definition 1.2.4. *A diffeomorphism from $\mathbb{R}^2$ to $\mathbb{R}^2$ which preserves area and orientation. Then F is called symplectic.*

The billiard map satisfies the twist condition which says the following:

Definition 1.2.5. *Let $f : (r, s) \to (\hat{r}(r, s), \hat{s}(r, s))$ be a symplectic map on the cylinder that is differentiable. Then f is a twist map if $\hat{s}$ is strictly increasing in r for any fixed s.*

A generating function is defined by Golé in [20] to be the following:

Definition 1.2.6. *Given a map $F(r, s) = (\hat{r}(r, s), \hat{s}(r, s))$, a function J is called a generating function for the lift of a twist map F if it has the following property:*

$$r = -\frac{\partial J(s, \hat{s})}{\partial s}$$

$$\hat{r} = \frac{\partial J(s, \hat{s})}{\partial \hat{s}}$$

The generating function for the billiard map is the distance function applied to two points on the boundary. We state and prove this with the following lemma.

Lemma 1.2.2. *Let*

$$J(s, \hat{s}) = |\tilde{B}(s) - \tilde{B}(\hat{s})|$$

where s and $\hat{s}$ are the arclength values. Then J is a generating function for the billiard map.

Proof. First note that $|\frac{dB}{ds}| = 1$ by definition of parametrization with respect to arc-length. Suppose that the angle between the line $B(\hat{s}) - B(s)$ and the tangent line is γ. Also note that $\frac{\partial \tilde{B}}{\partial s}$ is the tangent to $\tilde{B}$. Keeping in mind that the cosine formula for the dot product is as follows:

$$\left\langle \left(\tilde{B}(\hat{s}) - \tilde{B}(s)\right), \frac{\partial \tilde{B}}{\partial s} \right\rangle = \left|\tilde{B}(\hat{s}) - \tilde{B}(s)\right| \left|\frac{\partial \tilde{B}}{\partial s}\right| \cos\gamma$$

We apply the chain rule to find $\frac{\partial J}{\partial s}$:

$$\frac{\partial J}{\partial s} = \frac{-1}{2\sqrt{(x(s)-x(\hat{s}))^2+(y(s)-y(\hat{s}))^2}}\left(2(x(s)-x(\hat{s}))\frac{dx}{ds}+2(y(s)-y(\hat{s}))\frac{dy}{ds}\right)$$

$$= \frac{1}{|B(s)-B(\hat{s})|}\left\langle -(B(\hat{s})-B(s)) \ , \ \frac{dB}{ds}\right\rangle$$

$$= -\left|\frac{dB}{dt}\right|\cos\gamma$$

$$= -\cos\gamma = -r$$

Similarly we can find $\frac{\partial J}{\partial \hat{s}}$:

$$\frac{\partial J}{\partial \hat{s}} = \cos\gamma = \hat{r}$$

If we let $r = \cos\gamma$ then we have:

$$\frac{\partial J}{\partial s} = -r$$

$$\frac{\partial J}{\partial \hat{s}} = \hat{r}$$

This completes the proof. □

While we are not using the symplectic structure in our methods, this structure determines the type of dynamics we can expect. When parametrized by arc length, the billiard map is a homeomorphism as well with a proof outlined in [16]. Therefore, these properties underlie our analysis. Our billiard map takes $f : I \to I$ where $I = (-1,1) \times [0,1)$. This is also a homeomorphism. In the next section, we will discuss the billiard map on a few different tables as well as discuss the phase space structure for each table.

1.3 Table Shapes

We now focus on some specific smooth billiard domains, mainly the circle and the ellipse.

1.3.1 Billiards on Circular Tables

We start by considering a circular boundary. We use the equation for the circle with radius a parametrized, $\theta \in [0, 1)$:

$$B(\theta) = \begin{pmatrix} a\cos 2\pi\theta \\ a\sin 2\pi\theta \end{pmatrix} \tag{1.3}$$

Due to the symmetry of the circle, there is an explicit equation for the ball's trajectory. In the next lemma, we show that we can use rotation matrices to parametrize the curve to prove this explicit formula. In most literature, a geometric proof is used, as will be discussed after the following lemma.

Lemma 1.3.1. *For a circular table of radius a given by $B(\varphi) = (a\cos\varphi, a\sin\varphi)$ where $\varphi \in [0, 2\pi)$, let γ be the angle of the bounce and recall that $r = \cos\gamma$. Then,*

$$f(r, \varphi) = (r, \varphi + 2\gamma)$$

Proof. Suppose we are given an initial point on the circle $B(\varphi)$ with trajectory v. The angle γ, given in radians is the angle that the initial trajectory, v, of the particle makes with the tangent line at $B(\varphi)$ with $r = \cos\gamma$. The tangent vector at any given point on the circle is given by:

$$T(\varphi) = B'(\varphi) = \begin{pmatrix} -a\sin\varphi \\ a\cos\varphi \end{pmatrix}$$

We start with the initial point on the boundary at $\frac{-\pi}{2}$ with direction v, since γ would be measured off the horizontal at $B(-\frac{\pi}{2})$:

$$v_{\frac{-\pi}{2}} = \begin{pmatrix} \cos\gamma \\ \sin\gamma \end{pmatrix}$$

We can rotate any vector by $\theta + \frac{\pi}{2}$ to shift it from this point of reference at $\frac{-\pi}{2}$. This gives the following rotation matrix:

$$M = \begin{bmatrix} \cos\left(\varphi + \frac{\pi}{2}\right) & -\sin\left(\varphi + \frac{\pi}{2}\right) \\ \sin\left(\varphi + \frac{\pi}{2}\right) & \cos\left(\varphi + \frac{\pi}{2}\right) \end{bmatrix} = \begin{bmatrix} -\sin(\varphi) & -\cos(\varphi) \\ \cos(\varphi) & -\sin(\varphi) \end{bmatrix}$$

We can now find v given φ and γ. Using relations of sine and cosine, in particular, the additive angle identities, we find:

$$v = M \begin{pmatrix} \cos\gamma \\ \sin\gamma \end{pmatrix} = \begin{pmatrix} -\sin\left(\varphi + \gamma\right) \\ \cos\left(\varphi + \gamma\right) \end{pmatrix}. \tag{1.4}$$

Then, we find the next intersection point with the boundary by creating a straight line connecting $B(\varphi)$ and $B(\hat{\varphi})$ parametrized by some value s:

$$B(\hat{\varphi}) = B(\varphi) + sv. \tag{1.5}$$

Rewriting this in terms of our equation for B:

$$(a\cos\hat{\varphi},\ a\sin\hat{\varphi}) = (a\cos\varphi, a\sin\varphi) + s\cdot(-\sin\left(\varphi+\gamma\right), \cos\left(\varphi+\gamma\right))$$

and so we have:

$$a \cos \varphi - s \sin (\varphi + \gamma) = a \cos \hat{\varphi}$$

$$a \sin \varphi + s \cos (\varphi + \gamma) = a \sin \hat{\varphi}.$$

Summing the squares of these equations gives:

$$\begin{aligned}
(a \cos \varphi - s \sin (\varphi + \gamma))^2 + (a \sin \varphi + s \cos (\varphi + \gamma))^2 &= a^2 \\
a^2 + s^2 + 2as (\sin \varphi \cos (\varphi + \gamma) - \cos \varphi \sin (\varphi + \gamma)) &= a^2 \\
2as (\sin \varphi \cos (\varphi + \gamma) - \cos \varphi \sin (\varphi + \gamma)) &= s^2 \\
-2a \sin (\gamma) &= s.
\end{aligned}$$

Now we plug in the value for s back into equation (1.5) we get:

$$a \cos \hat{\varphi} = a \cos \varphi - 2a \sin (\gamma) \sin (\varphi + \gamma)$$

$$a \sin \hat{\varphi} = a \sin \varphi + 2a \sin (\gamma) \cos (\varphi + \gamma).$$

and substituting in the sum of angles formulas for the cosine and sine term with the $\varphi + \gamma$ argument and a lot of simplification we finally get:

$$a \cos \hat{\varphi} = a \cos (\varphi + 2\gamma)$$

$$a \sin \hat{\varphi} = a \sin (\varphi + 2\gamma)$$

Therefore, $\hat{\varphi} = \varphi + 2\gamma$. Now to find $\hat{r}$. Let U be the unit tangent at the new point of contact, $B(\hat{\varphi})$. Then U is given by the following:

$$U = \left(-\sin(\varphi + 2\gamma),\ \cos(\varphi + 2\gamma)\right).$$

Then using the dot product between v defined in equation 1.4 and U we find the expression for the cosine of the angle made between them, or in other words the angle of incidence made at $B(\hat{\varphi})$:

$$\begin{aligned}
\hat{r} &= \langle v, U\rangle \\
&= [-\sin(\varphi+\gamma)\sin(\varphi+2\gamma) + \cos(\varphi+2\gamma)\cos(\varphi+\gamma)] \\
&= [\cos((\varphi+\gamma) - (\varphi+2\gamma))] \\
&= \cos(\gamma) \\
&= r.
\end{aligned}$$

Note that this used the fact that v and U are unit length. The angle of incidence is the angle of reflection and thus $\hat{r} = r$. This completes the proof.

□

A more standard proof for this description of the circle billiard system is done with geometry. A picture for this idea can be seen in figure 1.4. We start by connecting the normal vectors at each of the endpoints of $\vec{v}$ to the center of the circle. We have thus constructed a triangle with the two normal vectors and $\vec{v}$ as the three sides. Since each of the normal vectors have length 1, we have constructed an isosceles triangle. Therefore, the angles made between each normal and v are equal, more specifically, they equal $\frac{\pi}{2} - \gamma$. Therefore, the angle made with v and the tangent at $B(\hat{\varphi})$ is γ. To find $\hat{\varphi}$, we simply need to add up the interior angles of the triangle:

$$\hat{\varphi} - \varphi + 2\left(\frac{\pi}{2} - \gamma\right) = \pi$$

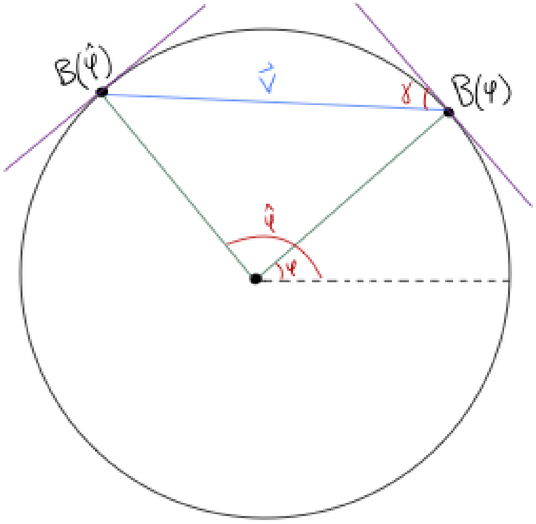

Figure 1.4: By constructing a triangle with the vector v (blue) and the normal vectors (green) at the two endpoints of v, we get an isosceles triangle. Implying that v makes the same angle with the two tangent vectors (purple).

and solving for $\hat{\varphi}$ gives:

$$\hat{\varphi} = \varphi + 2\gamma.$$

Given the simple map, it is easy to recognize periodic orbits. For example, when $r = 0$ a 2 -period orbit arises since that implies that $\gamma = \frac{\pi}{2}$ and $\hat{\varphi} = \pi$. Furthermore, when $\gamma = \frac{\pi}{4}$ we get $\hat{\varphi} = \varphi + \frac{\pi}{2}$ and is a periodic orbit with period 4. In fact, it is easy to see that when γ is rational, the orbit is periodic. When γ is irrational, the $\omega-$limit set of the orbit is the whole line. Therefore the phase space for the billiard map on the circle is a cylinder that only consists of horizontal invariant curves since r is constant. This was first shown by Birkhoff in [1].

The following corollary gives a similar result as lemma 1.3.1 for our definition of the circle table in equation (1.3). This way of describing the table is more in line with how we parametrize the table in the next few sections.

Corollary 1.3.1. *For a circular table of radius* a *given by* $B(\theta) = (a\cos(2\pi\theta), a\sin(2\pi\theta))$ *for* $\theta \in [0, 1)$,

$$f(r, \theta) = \left(r, \theta + \frac{\gamma}{\pi}\right),$$

where γ *is given in radians as defined in equation 1.2.2.*

1.3.2 Billiards on Elliptical Tables

Now we turn our attention to the ellipse. Given a smooth ellipse as the boundary for our table, we construct $B(\theta) = (x(\theta), y(\theta))$ where:

$$\begin{aligned} x(\theta) &= a_1 \cos 2\pi\theta \\ y(\theta) &= b_1 \sin 2\pi\theta. \end{aligned} \tag{1.6}$$

The goal is now to find an explicit expression for the next point of contact with the boundary. We can construct this explicit expression by writing the function for the line connecting $B(\theta)$ to $B(\hat{\theta})$ given by $v = (v_1, v_2) = B(\hat{\theta}) - B(\theta)$. We can now parametrize this line in the following way. For convenience, let $d_1 = \frac{v_1}{a}$ and $d_2 = \frac{v_2}{b}$.

$$\begin{aligned} \hat{x} &= x + sv_1 \\ \hat{y} &= y + sv_2. \end{aligned}$$

That is,

$$B(\hat{\theta}) = B(\theta) + sv, \tag{1.7}$$

i.e:

$$\cos 2\pi\theta_2 = \cos 2\pi\theta_1 + d_1 s$$

$$\sin 2\pi\theta_2 = \sin 2\pi\theta_1 + d_2 s.$$

Plugging these equations into the standard equation for the ellipse we get:

$$1 = (\cos 2\pi\theta_1 + sd_1)^2 + (\sin 2\pi\theta_1 + sd_2)^2$$

$$= 1 + 2s\,(d_1 \cos 2\pi\theta_1 + d_2 \sin 2\pi\theta_1) + s^2(d_1^2 + d_2^2).$$

Rearranging this equation gives us an explicit description for s:

$$s = -2\left(\frac{d_1 \cos 2\pi\theta_1 + d_2 \sin 2\pi\theta_1}{d_1^2 + d_2^2}\right).$$

We can then easily substitute this value for s back into the original parametrization to find the next point of impact on the boundary of the table.

The phase space for the ellipse, similar to the circle, consists only of invariant curves, see Figure 1.5. Which leads us into the Birkhoff conjecture. We now define what it means for a billiard system to be completely integrable. There are two ways to define integrability but we use the definition as found in [5].

Definition 1.3.1. *We say a billiard system is completely integrable if the phase space has a continuous full measure foliation by one-dimensional invariant submanifolds.*

In other words almost every point in the phase space is contained in a one dimensional invariant submanifold and those submanifold vary continuously with respect to some foliation parameter. Note that in the definition above the one dimensional submanifolds generally consist of more than one orbit. For continuously differentiable domains, the examples given so far fit this criteria. Billiards in a square domain are also completely integrable but we are focused on continuously differentiable domains. The dynamics in such a system is completely regular, [9]. This leads us to the Birkhoff conjecture with the earliest statement being made by Poritsky in 1950, [22], but we will use the statement summary given in [4].

Theorem 1.3.1 (Birkhoff Conjecture)**.** *For a convex smooth boundary, if the billiard system is completely integrable, it must be an ellipse.*

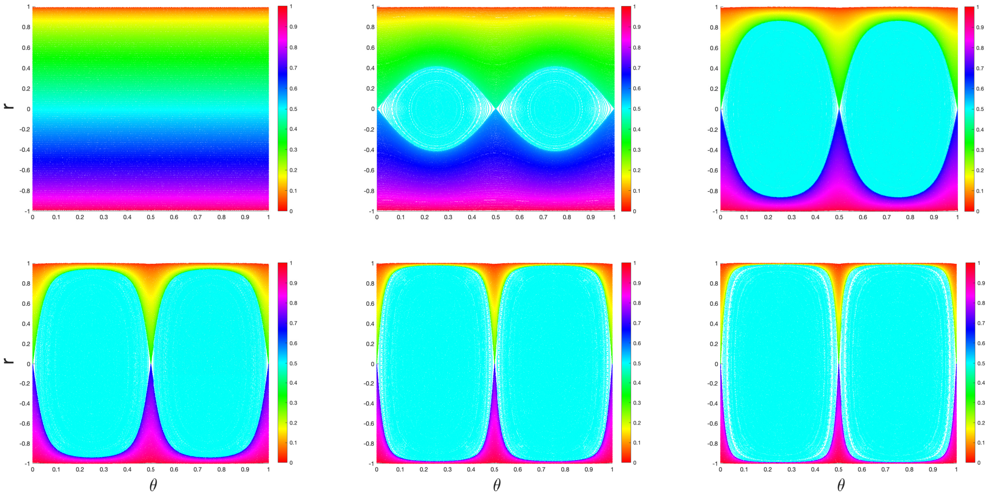

Figure 1.5: Phase space for the ellipse with $b_1 = 1$ and $a_1 = 1$ (top left), $a_1 = 1.1$ (top middle), $a_1 = 2$ (top right), $a_1 = 3$ (bottom left), $a_1 = 5$ (bottom middle), and $a_1 = 7$ (bottom right). Each orbit is colored by its rotation number, defined by definition 1.6.3 in section 1.6.1. This figure was made using 800 initial r values were taken from $\theta = 0.25$ and $\theta = 0.5$ each having orbit length 2000.

Research in billiards since then has been targeted towards proving this conjecture. For instance, in 1995, Delshams and Ramírez-Ros proved that any non-trivial, symmetric perturbation of the ellipse is not integrable, [3]. In [2], Avila et al. proved the Birkhoff conjecture for tables that are perturbed ellipses with small eccentricity. Then extended in [23] by Kaloshin and Sorrentino. In [24], Bialy and Mironov proved the Birkhoff conjecture for centrally-symmetric $\mathcal{C}^2$-smooth convex planar billiards.

Relating Dynamics to the Physical Table

There are a few notable aspects of the phase space for the ellipse. The phase space for several different ellipses can be found in figure 1.5. One can categorize each trajectory on the physical table into three separate groups of the phase space.

Theorem 1.3.2. *In the billiard system for an ellipse, if the initial trajectory of the ball is between the two foci of the ellipse, then each subsequent bounce will pass between the foci. These trajectories correspond to the bounded orbits in the phase space that lie on contractible circles when viewing the phase space as a cylinder.*

In figure 1.5, these orbits can be seen as the light blue circles. These types of orbits can be seen more explicitly in figure 1.1 as the purple and gold orbits. Figure 1.5 is colored by rotation number, which will be defined in section 1.6. For the ellipse, the rotation number can be taken to be the average amount of the table traversed by each bounce. As the eccentricity of the ellipse grows, these contractible circles grow as well, implying that more of the boundary can be reached if the trajectory passes initially between the foci. Another group of orbits exists in the ellipse, as follows.

Theorem 1.3.3. *In the billiard system for an ellipse, if the initial trajectory of the ball passes between a focus and the boundary of the ellipse, then each subsequent bounce will be directed between a focus and the boundary of the ellipse. These orbits correspond to the non-contractible orbits in the phase space when viewing the phase space as a cylinder.*

In figure 1.5, these orbits are represented by the curves above and below the contractible circles. This behavior is seen explicitly in figure 1.1 exhibited by the orange orbit. If the orbits have an irrational rotation number, the orbit will be a dense set. There exists one more type of orbit for the ellipse.

Theorem 1.3.4. *In the billiard system for an ellipse, if the initial trajectory of the ball passes through a focus of the ellipse, then each subsequent bounce will also pass through a focus of the ellipse. These orbits correspond to heteroclinic orbits in the phase space.*

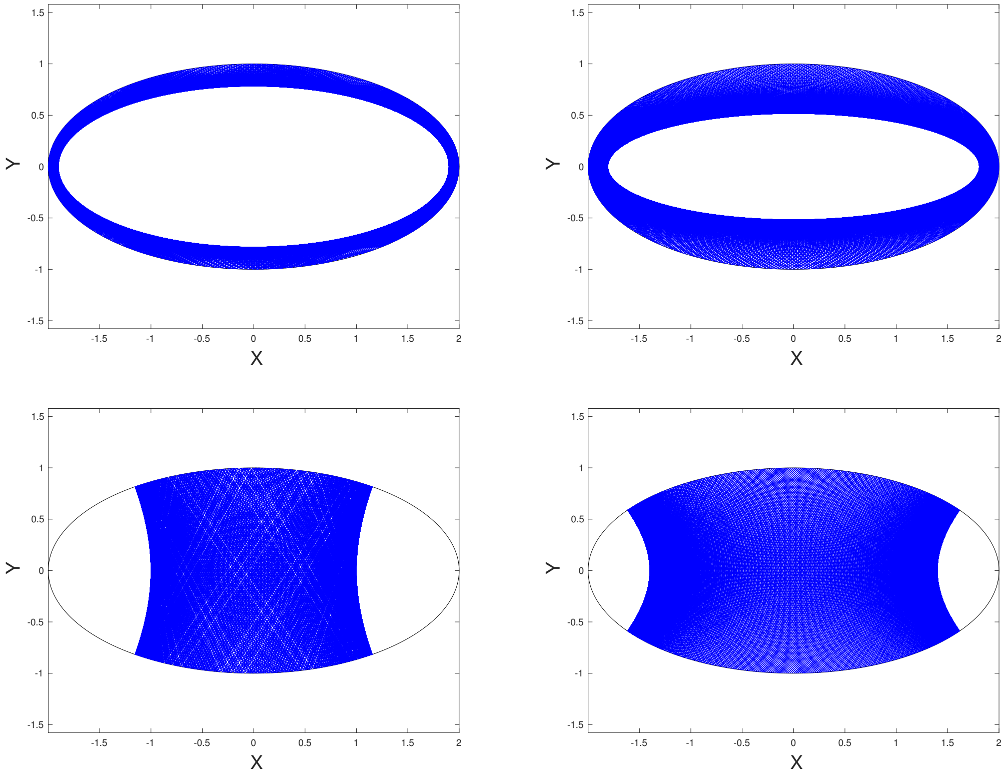

Figure 1.6: Caustic curves for the ellipse. For each picture, a single orbit was taken with orbit length 1000. The edge of the blue regions are the caustic curve. For the top row, the curve is an ellipse because the trajectory passes initially between a focus and the boundary. For the bottom row, the caustic curve is a hyperbola because the initial trajectory passes between the foci.

In figure 1.5, these orbits are represented by the ∞ shape that confines the contractible circles. Proofs for the above theorems can be found in [9] and in [25]. These groupings of orbits in the physical table are bounded by curves that are called caustics. Caustic curves are defined in the same way as Tabachnikov in [25].

Definition 1.3.2 (Caustic). *A caustic for a planar billiard orbit is a curve in $\mathcal{D}$, the physical table, such that if a trajectory is tangent to it, then it remains tangent to it after every reflection.*

Lazutkin in [26] proved that billiards in strictly convex, smooth boundaries have caustics. Mather was able to show that when the curvature of the boundary vanishes at some point, then no caustics exist in [27]. Caustic curves are not guaranteed to exist for every orbit in a general convex domain. One can see that no caustic exist for the gold orbit in the perturbed ellipse case shown in figure 1.1. The orbits that follow the criteria from theorem 1.3.2 are bounded by a hyperbola, this can be seen more clearly by the second row of figure 1.6. The orbits that follow the criteria from theorem 1.3.3 are each bounded by an ellipse which can be seen in the first row of figure 1.6. Lastly, the previous two groupings of caustics can be separated in the phase space by a heteroclinic orbit that is given by the orbits passing through the foci. A more in depth discussion of caustics of the ellipse can be found in [25].

1.3.3 Other Tables

Billiards tables consist of three types of curves that can make up their boundary: dispersing curves which are concave, focusing curves which are convex, and straight lines. In this thesis we will be focused on strictly focusing curves, hence the convex restriction in definition 1.2.2. With dispersing curves and straight lines, an issue arises in the construction of these table with the formation of discontinuous points on the boundary, namely, cusps and corners. For a more detailed discussion on the differences in these types of curves refer to [9].

When it comes to polygonal boundaries, the domain is taken to be a union of straight lines, connected at a single point. An introduction to billiards in the square can be found in [9] and an introduction to billiards for more general regular polygon tables can be found in [25]. The billiard map for regular polygons can be seen rather easily by tiling the plane with the boundary and drawing a straight line across the plane and keeping track of the orientation of each of these tiles. This process of tiling the plane is called unfolding. For a more robust description of unfolding see Gutkin, [28]. Although polygonal domains are not chaotic, they do display mixing properites, which is numerically demonstrated in recent research by do Carmo and Lima in [29].

Originally, it was thought that chaos was only present in tables with dispersing boundaries, but this was proved incorrect by Bunimovich in the mid 1970s. In [8], Bunimovich was able to show that there were tables with domains with boundary components consisting of only focusing curves and straight lines. These tables, referred to as Bunimovich tables, are domains with focusing components on the boundary that exhibit chaotic behaviour. An introduction to Bunimovich tables can be found in chapter 8 of [9].

1.4 Prior Numerical Methods for Billiards Systems

Many numerical methods have been used in previous research to simulate billiards systems. The goal of which is to accurately predict the next bounce for the orbit of a billiard ball within the billiard table. In this section, we describe some methods that have been proposed or used to model these systems, whether it be strictly using numerics in the physical space and some using numerics in the phase space.

1.4.1 Methods Using the Minimization Property

In [17], Levi and Tabachnikov utilize the minimization property to find the point of next contact of the particle with the boundary. An advantage for this method is that we can still use the parametrized curve representation for the ellipse. Furthermore, the method is quick to compute having only one instance of Newton's method to perform. This method relies on the fact that the table is convex and is not applicable for nonconvex tables. This method is particularly useful when discussing Poncelet polygons. More on Poncelet Polygons can be found in [17, 30]. For an introduction to the Poncelet theorem, refer to [25].

We originally attempted to implement this method with our billiard system but ran into two issues. The first being it relies on the norm which is not analytic. Therefore, we would not be able to utilize this in the continuation. The second issue is that y is not the only critical point of this function. There is in fact another critical point. The second solution to the above equation would be $-y$, meaning if we were to apply Newton's method to find this value, it could converge to the wrong value. In order to get around this, we apply several methods outlined in section 1.5.

1.4.2 Tangent Method

In [31], da Costa et al describe billiard dynamics on oval-like tables where the polar equation:

$$R_W(\theta) = 1 + \epsilon \cos p\theta \tag{1.8}$$

is used as the boundary for their table and p is some integer taken to be 3 in this particular paper. In equation (1.8), when $\epsilon = 0$, the billiard table is a circle. But as ϵ grows, the table becomes more deformed, essentially growing three connected lobes. Then functions are constructed for the x and y coordinates using equation (1.8) similar to how we set up the circle and ellipse cases. The tangent method is then implemented to find the point of next contact with the boundary. The tangent method is an iterative method that begins by constructing a parametrized line between the first and second contact point. Then an intersection point is found between the line and the approximate circle, $R = 1 + \epsilon$, call it (X_e, Y_e). This approximation is used to find the angular position on the actual boundary, (X_a, Y_a) which will provide a good guess for the next step. Drawing a tangent line at the point of (X_a, Y_a), one finds the parameter value for which the original line intersects this new tangent line. The point of intersection becomes the new (X_e, Y_e) and then the steps are repeated until $|X_e - X_a|$ and $|Y_e - Y_a|$ are within some tolerance. The final point produced by this iterative method will be the next point of contact with the boundary. The method uses an explicit expression for solving for the parameter value for the intersection of the trajectory. Each approximate tangent line involves derivatives of these coordinate equations. We found that we could not use this method since this type of perturbation was specifically for the circle and the overall formulation was not analytic.

1.4.3 Using the Standard Equation of the Ellipse

Some numerical methods rely on the standard form for the ellipse, meaning:

$$\left(\frac{x}{a}\right)^2 + \left(\frac{y}{b}\right)^2 = 1 \tag{1.9}$$

For example, Turaev in [32], the ellipse was perturbed by adding a small sine term to equation (1.9). The method for finding the next point of contact begins with finding the initial vector for the billiard ball, v_0. It then follows the v incrementally by small steps along the line connecting the initial boundary point and the first contact point by creating a line from v. At each increment of v, the point is checked whether it lies within the boundary or outside the boundary. This is accomplished by plugging in the new increment of v, or v_i into the above equation and subtracting this from the equation (1.9) applied to v_0. If the difference is negative, then the ball must be still inside the boundary, and if the difference is positive, then the ball is outside the boundary. Turaev would then set up the boundary as a system of differential equations to solve for the arc length coordinate using a fourth order Runge-Kutta method.

1.4.4 Using Energy Functions

In 2015, Solanpää et al in [33] wrote a C++ package to simulate general nonconvex billiard systems in 2D tables with more general criteria, similar to what is stated in definition 1.2.1. In this paper, they cover the methods used to simulate models for various billiards and diffusion models including those with multiple charged particles and those subject to magnetic fields. For the billiards model, they use the separable Hamiltonian function to implement a split operator scheme where they approximate the propagator by some product of solution forms for each of the parts in the separable Hamiltonian. Their software package is able to create phase spaces and single particle orbits for tables as easy as the ellipse to more complicated structures such as the Bunimovich mushroom.

1.4.5 Tables with Corners

Lansel and Proterin [34] wrote software to simulate classical billiard systems on tables that are constructed entirely of line segments but not necessarily convex. Their method focuses on tracking the trajectory of the ball v and the angle the ball makes with the horizontal axis, θ rather than tracking the cosine of the angle v makes with the tangent. From these values, they are able to to find the Cartesian coordinates for the point of contact on the boundary. Their method for solving for the next point of contact is slightly more complicated due to the more complicated structure of the table. They are given an initial point on the boundary and a trajectory v, then they find the intersection of v with each line segment that comprises the boundary. The intersection with the minimum distance is the next point of contact with the boundary. One issue that arises with tables comprising of line segments is corners, or the point where two line segments meet. There is no clear derivative at these points so they average the derivatives at the points to the right and left of the corner. This averaged derivative is then taken as the approximate derivative for the corner. I suspect this method could be applied to tables with smooth boundaries that are non-convex in combination with our method in the next section.

1.5 Methods for the Perturbed Ellipses

For the circle and ellipse, we have shown there are closed form solutions for describing the billiard balls path by the points of collision and the angles made with the tangent of the boundary. For general convex tables, there is no explicit solution. We now develop an implicit method to find these quantities.

1.5.1 Iterative Method of Real Valued Billiard Systems

Begin by defining a few variables in this system.

Definition 1.5.1. *Let* $B(\theta) = (x(\theta), y(\theta))$ *be a twice differentiable continuous boundary curve in* $\mathbb{R}^2$ *with counter-clockwise orientation where* $\theta \in [0, 1)$ *and* $B(0) = B(1)$. *Let* $T(\theta) = B'(\theta)$ *be the tangent vector to the curve. Given a point* θ *and an angle* γ, *let* v *and* r *be as follows:*

1. v *is the vector so* γ *is the angle between* v *and* T *as in section 1.2.*

2. $r = \cos \gamma$.

We focus on the case of the perturbed ellipse. In particular, we assume $B(\theta) = (x(\theta), y(\theta))$ is given by:

$$\begin{aligned} x(\theta) &= a_1 \cos(2\pi\theta) + \sum_{k=2}^{n} a_k \cos(2k\pi\theta) \\ y(\theta) &= b_1 \sin(2\pi\theta) + \sum_{k=2}^{n} b_k \sin(2k\pi\theta). \end{aligned} \tag{1.10}$$

As long as $(a_k, b_k) \ll (a_1, b_1)$, this is a small perturbation and additionally the table remains convex. We start with a point given by (r, θ). This implicitly defines a vector, v, as we see below.

Let $T(\theta) = B'(\theta)$ the tangent direction. Since orientation is counter-clockwise, the inward normal vector is given by $n(\theta) = (-T_2, T_1)$. Using the following dot product relation

$$a \cdot b = |a||b| \cos\theta$$

for two arbitrary vectors a and b, and the fact that γ is the angle between v and T, we get

$$\langle T(\theta), v\rangle = |T(\theta)|\,|v|\,r.$$

This does not have a unique solution since v can be of any length and still be a solution to the above equations, so we need another condition. The condition we choose to enforce is $\|v\| = 1$. Now we have a set of equations that will give a unique v. We write it in component-wise form:

$$\begin{aligned} T_1 v_1 + T_2 v_2 &= \sqrt{T_1^2 + T_2^2}\ r \\ v_1^2 + v_2^2 &= 1 \end{aligned} \tag{1.11}$$

noting that the $|v| = 1$ on the right hand side of the first equation.

Because of the square root, this set of equation (1.11) is non-analytic. We will need to fix this issue when moving to the complex plane in the future sections. This implicit equation for v can be written as a zero finding problem that can be solved, for example, with Newton's method.

Now that we have the vector v, we can use it to develop a method to find the next point of collision with the boundary. We start by constructing the line in the direction of v

$$L(s) = p_1 + sv, \tag{1.12}$$

where $p_1 = B(\theta_1)$ and s is a length parameter. Since the table is convex, this line has two intersection points with the boundary, the first being the original point the particle is leaving $B(\theta)$, and the second being the next point of contact $B(\hat{\theta})$. As long as we have a good guess near the desired solution, this intersection can be formulated as another zero finding problem when we construct the equation

$$F(s, \hat{\theta}) = L(s) - B(\hat{\theta}) = \begin{bmatrix} x_1 + sv_1 - \left(\sum_{k=1}^{n} a_k \cos\left(2\pi k\hat{\theta}\right)\right) \\ y_1 + sv_2 - \left(\sum_{k=1}^{n} a_k \sin\left(2\pi k\hat{\theta}\right)\right), \end{bmatrix} \tag{1.13}$$

which gives location of the next bounce on the boundary. The method we use to find this zero is Newton's method. Notice there are two zeroes that satisfy this equation, namely the new point $B(\hat{\theta})$ and the original point $B(\theta)$. Converging to the second bounce point is a matter of feeding in a good initial guess. We now explain how to find a good guess.

For a good guess we use two tactics. First we approximate the boundary by ellipse to be the ellipse generated by the first cosine and sine term in equation (1.10). Since predicting the next point of contact on an ellipse has closed form solution, we can find the next bounce on the approximate ellipse with the (r, θ) from the perturbed ellipse. Although, this next point on the approximate ellipse provides a good guess in most cases, it is not enough to guarantee convergence to the correct root in some small number of cases. These difficult cases occur when the ball only bounces a short distance, or more specifically r is close to 1. In order to converge to the correct root in these cases, we use the method of *deflation* on the function $F(s, \hat{\theta})$ to eliminate the incorrect zero we do not want Newton's method to converge. We will discuss this in more detail in section 1.5.4.

After we have found the next point of contact, $B(\hat{\theta})$, we now need the new $\hat{r}$. Since we now know $\hat{\theta}$ we can find the tangent line at this point, $U(\hat{\theta}) = B'(\hat{\theta})$. From theorem 1.2.1, we know that the angle made by v_2 with the tangent line will be the same as the angle between v_1 and the tangent line. Thus, using the dot product relation with the angle we get:

$$\hat{r}^2 - \frac{(v \cdot U)^2}{\|U\|^2} = 0 \tag{1.14}$$

which becomes yet another implicit equation which can be solved by using Newton's method. This completes the method.

This method was implemented to create figures 1.7, where we slowly increase the second terms by some parameter ϵ in each of the coordinates. Using the weighted Birkhoff average, we are able to subtract out the chaotic regions. This will be explained in more detail in section 1.6.

A question that may arise from the way we perturb the ellipse is given the coefficients in figure 1.7, what value of ϵ will cause the table to not be convex. To answer this, we calculated the signed curvature. For the general curve close curve $B(\theta) = (x(\theta), y(\theta))$

$$k = \frac{x'y'' - y'x''}{(x'^2 + y'^2)^{\frac{3}{2}}}.$$

If the curve bounds a convex set then k is always positive. If the curve bounds a concave set, then the minimum k is negative. We calculated the minimum k value for tables associated with coefficients $a_1 = 1.1$. $a_2 = 0.03\epsilon$, $b_1 = 1$, and $b_2 = 0.25\epsilon$ and found that the maximum

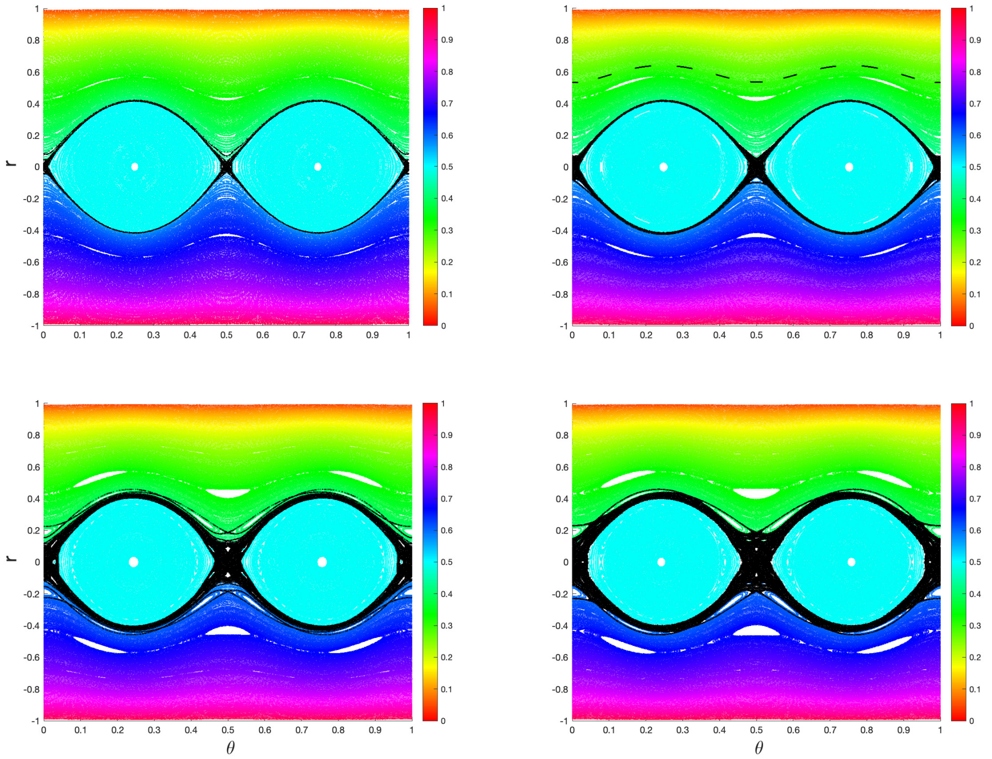

Figure 1.7: Phase space for the billiard map on the perturbed ellipse given by equation (1.10) with coefficients $a_1 = 1.1,\ a_2 = 0.03\epsilon$, $b_1 = 1$, and $b_2 = 0.025\epsilon$ where ϵ is varied between 0.1 and 1. The color of each orbit represents the rotation number for the orbit. The chaotic orbits are in black. Each picture was created by taking 600 initial r values for each $\theta = 0,\ 25,\ 0.33,\ 0.4$ and 0.5. Each orbit has length 2000.

epsilon one could have without the curvature being less than zero is about $\epsilon = 9.1806$. Beyond this value, the table fails to be convex. This can be seen in figure 1.8. Figure 1.8 also shows the calculation of minimum signed curvature for each ϵ value. If one wished to perturb the ellipse to have more terms, then an easy guess would be to make each $a_n, b_n = 10^{-n}\epsilon$. Then the maximum ϵ value above would remain the largest epsilon value for the table to remain convex.

1.5.2 An Analytic Method for Continuation

We now develop an analytic method for computing billiard maps. Unlike our previous method, we require a guess for the iterate of the point. Thus, this method will be effective

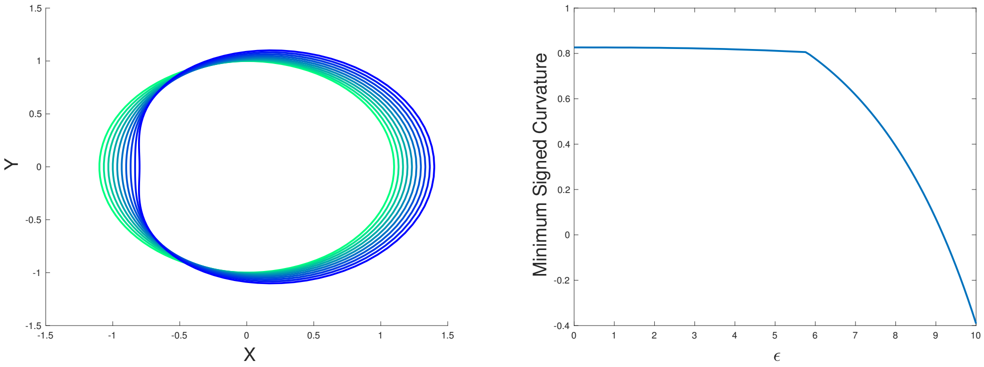

Figure 1.8: Calculating the maximum ϵ value for the table to remain convex using the coefficients used to produce figure 1.7. The picture on the right shows the table deforming due to the change in ϵ. While the picture on the left shows the calculation for the minimum signed curvature calculated for each ϵ.

for continuation but not for finding big orbits. In this section, we propose a predictor-corrector continuation method to push our phase space into complex space. The reason we want to use a real analytic function is that we need a way to compute f applied to a Taylor series and get another Taylor series. Since the map is defined implicitly the most accurate way to this is to evaluate f of the Taylor series at the nth roots of unity and take the discrete Fourier transform. The method is as follows: We begin by predicting the next point of contact with the boundary by using the real case. Then we continue by using a nearby complex solution as a guess for the new complex one. We start by assuming the definition 1.5.1 from section 1.5, but now we have that the (r, θ) has real and imaginary parts.

As previously done, we first need to find the vector v, which is the vector that is at an angle γ with the tangent line at $B(\theta)$. Previously, we used the dot product formula, but this no longer works in the complex case since it requires taking the square root of a complex value. Therefore, the system will not be analytic. To get around this we square both sides of the equation and keep the requirement that v has modulus 1. This yields the set of equations

$$
\begin{aligned}
&(T_1 v_1 + T_2 v_2)^2 = (T_1^2 + T_2^2) r^2 \\
&v_1^2 + v_2^2 = 1
\end{aligned}
\tag{1.15}
$$

From this we move the left terms to the right hand side of the equation and apply Newton's method to find the v that is the zero for the system. Once we have the trajectory of the ball v, we can move onto the next step, finding the next point of contact with the boundary, $B(\hat{\theta})$. To do this we perform the same step as the real case by constructing the function

$$L(s, \hat{\theta}) = B(\theta) + sv - B(\hat{\theta}). \tag{1.16}$$

We then apply Newton's method to this equation to find the zero for this function and get the parameter value $\hat{\theta}$ which corresponds to the next point of contact with the boundary. The difference between this step and its corresponding step in the real case is that we cannot apply deflation since our function might not be analytic. Therefore, this method would not work for small bounces.

Lastly, we need to compute $\hat{r}$, the cosine of the angle between the tangent at $B(\hat{\theta})$ and the new trajectory $\hat{v}$. As before, $U = B'(\hat{\theta})$ is the tangent vector at the point $B(\hat{\theta})$ and v is the initial trajectory of the particle pointing towards $B(\hat{\theta})$. Again, we perform the same step as the iteration method, solving the following equation:

$$\hat{r}^2 - \frac{(v \cdot U)^2}{|U|^2} = 0. \tag{1.17}$$

We perform these steps for each iterate of the billiard map with complex r and θ by taking the real components of $\hat{r}$ and $\hat{\theta}$ for the iteration method in the next step.

In the next section we will construct an implicit computation of the derivative for the map f which will be necessary for us to implement the parametrization method.

1.5.3 Finding the Derivative for the Billiard Map

In this section, we find Df. This will be used to implement some of the methods described in section 1.6 and section 1.7. More specifically, we need to find an expression for

$$\frac{\partial f}{\partial(r,\theta)} = \begin{bmatrix} \frac{\partial \hat{r}}{\partial(r,\theta)} \\ \frac{\partial \hat{\theta}}{\partial(r,\theta)} \end{bmatrix}. \tag{1.18}$$

We are able to do so by using implicit differentiation.

Start by defining $T(\theta) = B'(\theta)$ where $B(\theta)$ is the function that describes the table and DB is the derivative. The first step of our method requires finding $v = (v_1, v_2)$ given (r, θ), that satisfies

$$G(v_1, v_2, r, \theta) = \begin{bmatrix} (T_1(\theta)v_1 + T_2(\theta)v_2)^2 - \left(T_1(\theta)^2 + T_2(\theta)^2\right) r^2 \\ v_1^2 + v_2^2 - 1 \end{bmatrix} = 0. \tag{1.19}$$

Since G is dependent on v_1, v_2, r, and θ and, in fact, v_1, v_2 are dependent on r and θ, we can use implicit differentiation to find an expression for:

$$\frac{\partial(v_1, v_2)}{\partial(r,\theta)} = -\left(\frac{\partial G}{\partial v}\right)^{-1} \frac{\partial G}{\partial(r,\theta)}. \tag{1.20}$$

Therefore, we just need to find expressions for the two derivative matrices on the right side of the equation. Let $T(\theta) = B'(\theta) = (T_1(\theta), T_2(\theta))$ be the equation for the tangent line at the point $B(\theta)$ on the boundary of the table. Then, from equation (1.10)

$$T_1(\theta) = \sum_{k=1}^{n} -2\pi k a_k \sin(2\pi k\theta)$$

$$T_2(\theta) = \sum_{k=1}^{n} 2\pi k b_k \cos(2\pi k\theta).$$

The derivative with respect to θ of T is given by the following expression:

$$\frac{\partial T_1}{\partial \theta}(\theta) = \sum_k -(2\pi k)^2 a_k \cos(2\pi k\theta)$$

$$\frac{\partial T_2}{\partial \theta}(\theta) = \sum_k -(2\pi k)^2 b_k \sin(2\pi k\theta)$$

Now we have a formula for T and the derivative of T, which we will shorten to T', which will help give us a more explicit expression for $\frac{\partial G}{\partial(r,\theta)}$. Taking the partial derivative of G with respect to r and θ gives us the 2×2 matrix:

$$\frac{\partial G}{\partial(r,\theta)} = \begin{bmatrix} -2r(T_1^2 + T_2^2) & 2(T_1v_1 + T_2v_2)(T_1'v_1 + T_2'v_2) - 2(T_1T_1' + T_2T_2')r^2 \\ 0 & 0 \end{bmatrix}. \tag{1.21}$$

Taking the partial derivative of G with respect to v_1, v_2 gives the 2×2 matrix

$$\frac{\partial G}{\partial v} = \begin{bmatrix} 2(T_1v_1 + T_2v_2)T_1 & 2(T_1v_1 + T_2v_2)T_2 \\ 2v_1 & 2v_2 \end{bmatrix}. \tag{1.22}$$

Combining equations (1.20),(1.21), and (1.22), we can solve for $\frac{\partial v}{\partial(r,\theta)}$. In the next step of our method, we wish to find the $\hat{\theta}$. Let H be a function that is the the difference between the boundary and the trajectory of the ball we found in the previous step, v. Remember from the previous section, equation 1.13, that the zero for this function will be the point of next contact on the boundary $\hat{\theta}$ where

$$H(r,\theta,s,\hat{\theta}) = B(\theta) + sv - B(\hat{\theta}) = 0. \tag{1.23}$$

Notice here that H is dependent on r, θ, s, and $\hat{\theta}$ where $v = v(r, \theta)$ as above. Assume that s and $\hat{\theta}$ depends on r and θ. By implicit differentiation we get the expression

$$\frac{\partial(s, \hat{\theta})}{\partial(r, \theta)} = -\left(\frac{\partial H}{\partial(s, \hat{\theta})}\right)^{-1} \frac{\partial H}{\partial(r, \theta)}. \tag{1.24}$$

Notice that the second column of equation (1.24) is half of the matrix we need from equation (1.18). Taking the partial derivatives of H with respect to s and $\hat{\theta}$ yields the following 2×2 matrix:

$$\frac{\partial H}{\partial(s, \hat{\theta})} = \left(\begin{array}{c|c} v & -\frac{dB}{d\theta}(\hat{\theta}) \end{array}\right) \tag{1.25}$$

and now finding the partial derivative of H with respect to r and θ yields another 2×2 matrix

$$\frac{\partial H}{\partial(r, \theta)} = \left(\begin{array}{c|c} s\frac{\partial v}{\partial r} & \frac{dB}{d\theta}(\theta) + s\frac{\partial v}{\partial \theta} \end{array}\right). \tag{1.26}$$

Combining equations (1.24), (1.25), and (1.26) we now have an expression for $\frac{\partial(s,\hat{\theta})}{\partial(r,\theta)}$. The third and final step of our method is to compute the new $\hat{r}$ for our trajectory. Let $U = DB(\hat{\theta})$, the equation of the tangent line at $B(\hat{\theta})$. From equation (1.14) in the previous section, we can construct K to be a function of $r, \theta, \hat{r} \in \mathbb{R}$ such that

$$K(r, \theta, \hat{r}) = \hat{r}^2 - \frac{(U_1 v_1 + U_2 v_2)^2}{U_1^2 + U_2^2}. \tag{1.27}$$

We again, use implicit differentiation to find an expression for $\frac{\partial \hat{r}}{\partial(r,\theta)}$

$$\frac{\partial \hat{r}}{\partial(r, \theta)} = -\left(\frac{\partial K}{\partial \hat{r}}\right)^{-1} \frac{\partial K}{\partial(r, \theta)}. \tag{1.28}$$

Finding the solution to the right hand side of this equation will give us the final expression we need for the derivative of $\hat{r}$ with respect to r and θ. These partial derivatives have an explicit expression as well with one being a single value and the other a column vector:

$$\frac{\partial K}{\partial \hat{r}} = 2\hat{r} \tag{1.29}$$

and

$$\begin{aligned}\frac{\partial K}{\partial(r,\theta)} &= \frac{-2(U_1v_1+U_2v_2)}{U_1^2+U_2^2}\left(\frac{\partial U_1}{\partial(r,\theta)}v_1+\frac{\partial v_1}{\partial(r,\theta)}U_1+\frac{\partial U_2}{\partial(r,\theta)}v_2+\frac{\partial v_2}{\partial(r,\theta)}U_2\right)\\ &\quad+\frac{(U_1v_1+U_2v_2)^2}{(U_1^2+U_2^2)^2}\left(2U_1\frac{\partial U_1}{\partial(r,\theta)}+2U_2\frac{\partial U_2}{\partial(r,\theta)}\right).\end{aligned} \tag{1.30}$$

Thus we now have an expression for both $\frac{\partial \hat{r}}{\partial(r,\theta)}$ and $\frac{\partial \hat{\theta}}{\partial(r,\theta)}$, where

$$\frac{\partial \hat{r}}{\partial(r,\theta)} = -\left(\frac{\partial K}{\partial \hat{r}}\right)^{-1}\cdot\frac{\partial K}{\partial(r,\theta)} \tag{1.31}$$

and

$$\frac{\partial \hat{\theta}}{\partial(r,\theta)} = \left(-\left(\frac{\partial H}{\partial(s,\hat{\theta})}\right)^{-1}\cdot\frac{\partial H}{\partial(r,\theta)}\right)_2, \tag{1.32}$$

where $(\cdot)_2$ represents the second row of the matrix. Since $\frac{\partial \hat{r}}{\partial(r,\theta)}$ is a column vector, we will need to take the transpose of this vector and combine it with the row vector $\frac{\partial \hat{\theta}}{\partial(r,\theta)}$ giving us the final expression for the 2 × 2 matrix in equation (1.18).

Before we can show that the map f is analytic we will need help from the implicit function theorem. We state the theorem as shown in [35] which is the version of Hildebrandt and Graves.

Theorem 1.5.1. *Suppose that the mapping* $F : U(x_0, y_0) \subset X \times Y \to Z$ *is continuous and defined on an open neighborhood* $U(x_0, y_0)$ *and* $F(x_0, y_0) = 0$ *where* $X, Y,$ *and* Z *are Banach spaces over* $\mathbb{C}$*. Suppose further that the partial derivative* D_yF *exists on* U*, is continuous at* (x_0, y_0)*, and* $\det D_yF(x_0, y_0) \neq 0$*. Then the following are true:*

1. *There exists positive numbers* r_0 *and* r *such that for every* $x \in X$ *satisfying* $|x-x_0| \leq r_0$ *there is exactly one* $y(x) \in Y$ *for which* $|y(x) - y_0| \leq r$ *and* $F(x, y(x)) = 0$*.*
2. *If* F *is continuous in a neighborhood of* (x_0, y_0) *then* $y(x)$ *is continuous in a neighborhood of* x_0*.*
3. *If* F *is a* C^k *(analytic) map for* $1 \leq m \leq \infty$ *on a neighborhood of* (x_0, y_0) *then* $y(x)$ *is also a* C^k *(analytic) map on a neighborhood of* x_0*.*

From the above theorem we are able to prove the following result for our map f.

Theorem 1.5.2. *The billiard map* f *as defined in section 1.5.2 is analytic for* $r \in (-1, 0) \bigcup (0, 1)$ *and* $\theta \in [0, 1)$*.*

Proof. If G, H and K are analytic and satisfy the criteria of theorem 1.5.1 then so f is analytic as well. It is easy to see that these functions are analytic since G and K are polynomials in each term. H is analytic since it is a sum of analytic functions. Therefore, we just need to show that:

$$\det \frac{\partial G}{\partial v} \neq 0, \ \det \frac{\partial H}{\partial (s, \hat{\theta})} \neq 0, \quad \text{and } \frac{\partial K}{\partial \hat{r}} \neq 0.$$

First we take the determinant of equation (1.22) which is

$$4(T_1v_1 + T_2v_2)(T_1v_2 - T_2v_1).$$

which is non-zero as long as $\langle T, v\rangle \neq 0$ or when $\langle n, v\rangle = \langle(-T_2, T_1), v\rangle \neq 0$. The first case corresponds to when v is orthogonal to the tangent line at the point of contact or

$r = 0$ which we do not allow. The second case corresponds to when the normal vector is orthogonal to v. This would imply that v is in the same direction of the tangent or $r = -1$ or 1. This situation cannot occur due to our restrictions on the boundary.

Second we take the determinant of equation (1.25) and get

$$-v_1 B_2'(\hat{\theta}) + v_2 B_1'(\hat{\theta}) = \langle v, (-T_2, T_1) \rangle = \langle v, n \rangle .$$

The above is only equal to 0 when v is parallel to the normal vector at the point of next contact or, $\hat{r} = 0$. Lastly, for equation (1.29), we have

$$\frac{\partial K}{\partial \hat{r}} = 2\hat{r}.$$

We see that the inverse exists if and only if $\hat{r} \neq 0$. Therefore, we have that each map f exists and is continuous, differentiable, and analytic on $r \in (-1, 0) \bigcup (0, 1)$ and $\theta \in [0, 1)$.

$\square$

Our first instinct to solving this problem at $r = 0$ was to reformulate equation (1.15) to be the dot product with the normal vector of the boundary. Although this allows us to solve equation (1.15), we would still be unable to solve equation (1.17) since the derivative would be zero.

In summary, we now have a three step implicit method for finding an iterate of a billiard map as well as an expression for the derivative of this map. The key point of this method is that it is analytic but there are a few drawbacks to this method as well which we will discuss in the next section.

In section 1.6.2, we will discuss some results that use this derivative to find periodic orbits using a multiple shooting Newton's method, and in section 1.7 we will discuss how this derivative assists in computing the stable and unstable manifolds for these periodic orbits.

1.5.4 Numerical Issues

The strengths of this implicit formulation of the billiard map lie in its structure. For one, the way we construct this perturbation mimics the Fourier series where the advantage will become clear when implementing the parametrization method in section 1.7. One issue that arises with this construction mainly occur at $(r, \theta) = (0, 0)$ and $(r, \theta) = (0, 0.5)$. The orbit for this initial conditions is a two period orbit that bounces between these two points. Furthermore, the Jacobian is singular for equation (1.11) and (1.15) meaning, we cannot apply Newton's method. One more computational issue arises with equation (1.11) when Newton's method converges to v_{k-1}. In other words, it finds the previous v that is approaching the current point on the table. To rectify this, we use theorem 1.2.1 to find v_k.

Another issue that arises in the real case is with solving the equation (1.13). As stated in section 1.5, in cases where the ball is travelling a small distance along the boundary, our Newton's method converges to the point of origin rather than the point of next contact. To avoid this, we implement deflation. Deflation was originally applied to polynomial equations with roots that are wide spread by Peters and Wilkinson in [36]. Wilkinson deflation of polynomials was then extended to systems of nonlinear algebraic equations by Brown and Gearhart in [37]. Then extended to infinite dimensional Banach spaces by Farrel et al in [38] and extended to computing bifurcation diagrams by Beentjes in [39]. For a general non-linear function $F : X \to Y$, where X and Y are Banach spaces, deflation is defined as follows.

Definition 1.5.2. *The deflation matrix is*

$$M(x, r) = \frac{I}{|x - r|},$$

where I is the identity matrix.

Supposing that F has two roots x_1 and x_2 such that $F(x_1) = F(x_2) = 0$, then the deflation operator

$$T(x) = M(x, x_1)F(x)$$

will converge to the root x_2 using Newton's method. The proof of these statements can be found in [37] and [39]. We apply the deflation matrix to the equation (1.13) with $(s, \theta) = (0, \theta_i)$ where θ_i corresponds to the point on the boundary where the path of the ball starts. Therefore, we guarantee that Newton's method on equation (1.13) always converges to θ_{i+1}.

1.6 Applications for Iterative Methods

1.6.1 Chaos and Rotation Number

In this section we will define the rotation number and its properties. The results from computing the rotation number for some test cases as well as the billiard map will be in the following results section. Before we define the rotation number, we first define some preliminary definitions.

Definition 1.6.1. *Let $\Pi : \mathbb{R} \to S^1$ be the standard projection onto the circle. This can be represented in a couple of different ways:*

1. $\Pi(t) = t \mod 1$
2. $\Pi(t) = e^{2\pi i t}$

For our purposes, we will be using the first representation listed in equation 1.6.1. Now we state the definition for a lift as seen in [21].

Definition 1.6.2. *Suppose $f : S^1 \to S^1$ and is orientation preserving. Then a lift, $F : \mathbb{R} \to \mathbb{R}$, of f is a map such that:*

1. $\Pi \circ F = f \circ \Pi$

2. F is monotonically increasing

3. $F(t+1) = F(t) + 1, \quad \forall t.$

A lift is not unique. For example, for any homeomorphism f, if F_1 and F_2 are two lifts, then there exists an integer k such that $F_2(t) = F_1(t) + k$, [21].

Definition 1.6.3. *Let $f : S^1 \to S^1$ be a homeomorphism with lift $F : \mathbb{R} \to \mathbb{R}$. Let*

$$\hat{\rho}(f) = \lim_{n\to\infty} \frac{F^n(x) - x}{n}.$$

Then, the rotation number for the orbit of x is $\rho(x) = \hat{\rho} \mod 1$.

It is not obvious, but the rotation number is independent of the point, and is also independent of the lift. A proof of these statements can be found in [21]. The rotation number is rational when the orbit is periodic, as stated and proved in the following lemma.

Lemma 1.6.1. *If there is a point on $[0, 1]$ with least period $q \in \mathbb{N}$ then $\rho(F) = \frac{p}{q}$ where $p \in \mathbb{N}$.*

Proof. Suppose that $x \in [0, 1]$. Then, $F^q(x) = x + p$ for some $p \in \mathbb{Z}$. Let $n > q$ be an integer. Then n has a unique representation of the form

$$n = kq + r.$$

Therefore,

$$F^n(x) = F^{kq+r}(x) = F^r\left(F^{kq}(x)\right) = F^r(x + kp) = F^r(x) + kp.$$

Now using the definition of rotation number yields:

$$\lim_{n\to\infty} \frac{F^n(x) - x}{n} = \lim_{k\to\infty} \frac{F^r(x) + kp - x}{kq + r} = \frac{p}{q}.$$

□

The previous lemma implies that, if the orbit is periodic, then the rotation number will be rational. We generalize the above lemma to include irrational rotation numbers. The proof can be found in [21].

Theorem 1.6.1. *Suppose $f : S^1 \to S^1$ is a C^2 orientation preserving diffeomorphism. Then, for the rotation number λ, if:*

1. *λ is rational, then f has a periodic point. If it is not the periodic point, then the orbit will asymptotically approach the periodic point.*
2. *λ is irrational, then f is topologically conjugate to a rigid rotation*

$$G(x) = (x + \lambda) \mod 1.$$

We call such cases quasiperiodic.

Weighted Birkhoff Averages

In this section we describe how we find the weighted Birkhoff average, WBA, for an orbit. We found that this method was able to distinguish chaotic orbits from regular orbits, as well as to compute rotation number. After finding the appropriate length of the orbit to see this difference, as seen in 1.13, we are able to implement this method for the billiard map. In [40] and [41], Das et al. introduced WB_N as a method that can be efficiently applied to the computation of rotation numbers and conjugacies to rigid rotations for quasi-periodic systems. Suppose we have a probability space X with measure μ. We start with some definitions from [21].

Definition 1.6.4. *A measure μ is invariant for a map $f : X \to X$ provided $\mu(f^{-1}(A)) = \mu(A)$. If μ is an invariant measure for f, f is also said to be a μ-measure-preserving transformation.*

Definition 1.6.5. *A map* $f : X \to X$ *is called ergodic with respect to invariant measure* μ *provided* $\mu(X \setminus A) = 0$ *for any measurable invariant set* A *of* f *with* $\mu(A) > 0$.

With these two definitions, we can state the Birkhoff ergodic theorem as stated in [21].

Theorem 1.6.2 (Birkhoff's Ergodic Theorem)**.** *Assume* $f : X \to X$ *is a measure preserving transformation for the measure* μ. *Assume* $g : X \to \mathbb{R}$ *is a* μ*-integrable function. Then*

$$\lim_{T\to\infty} \frac{1}{T} \sum_{j=0}^{T-1} g \circ f^j(x)$$

converges μ*-almost everywhere to an integrable function* g^*. *Also,* g^* *is* f *invariant wherever it is defined for* μ*-almost all* x. *Furthermore, the following statements hold.*

(i) If $\mu(X) < \infty$ *then*

$$\int_X g^*(x) d\mu(x) = \int_X g(x) d\mu(x).$$

(ii) If μ *is an ergodic measure for* f, *then* g^* *is a constant* μ*-almost everywhere.*

This theorem implies that, if a μ-measure-preserving transformation is ergodic on a finite measure space, then the time average of an orbit is equivalent almost everywhere to its spatial average with respect to μ. In order to calculate this average, since taking this limit is computationally impossible, we take a finite time average for large T.

For any function $h : M \to \mathbb{R}$, a finite-time Birkhoff average on an orbit of a map f beginning at point $z \in M$ is given by

$$B_T(h)(z) = \frac{1}{T} \sum_{k=0}^{T-1} h \circ f^k(z). \tag{1.33}$$

If f is measure-preserving, letting T go to infinity, Theorem 2.1 guarantees this average converges almost everywhere. The problem with numerical implementation of equation

1.33 is that convergence is slow. More specifically, convergence for the Birkhoff average is of order $\mathcal{O}\left(\frac{1}{T}\right)$ for the quasi-periodic case where T is the length of the orbit [40]. The weighted Birkhoff average was introduced in [40] in order to speed up convergence. We will now explain the method of weighted Birkhoff averages.

We call a function $g : \mathbb{R} \to [0, \infty)$ a C^∞ weighting function if g is infinitely differentiable, $g > 0$ on $[0, 1]$, and $g = 0$ elsewhere. We can now define a weighted Birkhoff average

$$WB_T(h(z)) = \sum_{t=0}^{T-1} w_{t,T} h \circ f^t(z) \tag{1.34}$$

where

$$w_{t,T} = \frac{1}{S} g\left(\frac{t}{T}\right), \quad S = \sum_{t=0}^{t-1} g\left(\frac{t}{T}\right).$$

Our particular choice of $\mathcal{C}^\infty$ weighting function g is the exponential bump function

$$g(t) = e^{[-t(1-t)]^{-1}},$$

for $t \in (0, 1)$ and 0 everywhere else. The function g is chosen to be a function that is infinitely smooth at 0 and 1 to minimize the error caused by the ends of the orbit [42]. This method results in significant speed up of convergence for non-chaotic orbits but not chaotic orbits since the average does not converge for these orbits in the same amount of time. For chaotic orbits, the convergence can be arbitrarily slow, but is generally expected to be $\mathcal{O}\left(\frac{1}{\sqrt{T}}\right)$, due to the central limit theorem. Das and Yorke show in [41, 43] that if f and h are infinitely differentiable, then on non-chaotic orbits that meet the diophantine condition, the method has super polynomial convergence. See Theorem 1.6.2.

The method we use to determine chaos from regularity is as follows. For two segments of an orbit

$$\{1, ..., T\} \text{ and } \{T + 1, ..., 2T\},$$

we compute the weighted Birkhoff average for each and then compute the number of consistent digits beyond the decimal point in our two approximations,

$$\mathrm{dig}_T = -\log_{10} \left| WB_T(h)(z) - WB_T(h)(f^T(z)) \right|. \tag{1.35}$$

If dig_T is large, then convergence is fast, meaning the orbit is non-chaotic. If dig_T is small then convergence is slow indicating the orbit is chaotic. Therefore, the difference between these two weighted Birkhoff averages will have a large difference. If the orbit is quasi-periodic then the two weighted Birkhoff averages will be close, as stated in the following theorem.

Theorem 1.6.3. *Let f be a C^∞ map and let $\{f^t(z)\}$ be a quasi-periodic orbit with a Diophantine rotation number, and let h be a C^∞ function, then there exist constants c_n such that for all $n \in \mathbb{N}$,*

$$\left| WB_T(h)(z) - \lim_{N\to\infty} B_N(h)(z) \right| < c_n T^{-n}.$$

This method has previously been used as follows. In [44], Das et al. applied the method of weighted Birkhoff averages to compute rotation rates of quasi-periodic trajectories and applied the method to the planar three body problem with one mass being infinitesimal compared to the other two. These methods were extended to distinguish orbits that lie on rotational two-tori in [45]. Meiss and Sander applied weighted Birkhoff averages to a three dimensional analogue to Chirikov's standard map which will be defined in the next section. In [46], Duignan and Meiss extend these results to ergodic flows and applied the method to the two wave Hamiltonian system, a quasi-periodically forced, dissipative system that has a strange attractor with no positive Lyapunov exponents and a model for magnetic line flow. In [47], Blessing and James used the method of WBA to initialize the parametrization for invariant tori. They are able to do this by using the weighted Birkhoff average to determine the rotation number and conjugacy equation of the quasiperiodic system. In the

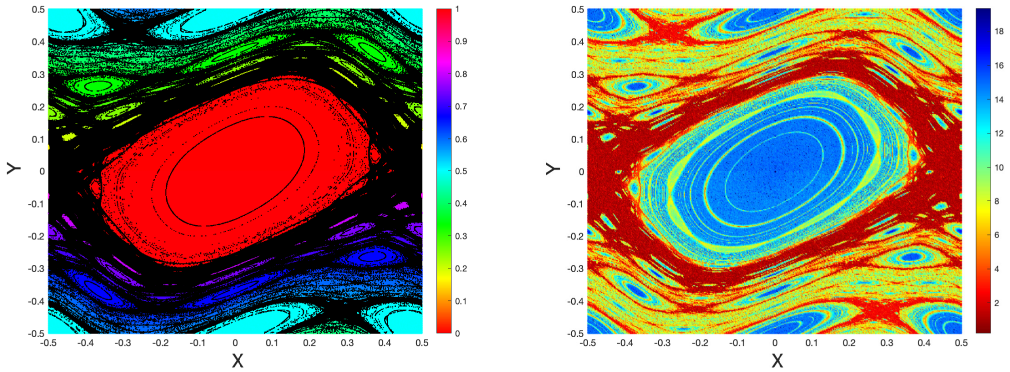

Figure 1.9: Phase space for the Chirikov standard map defined by equation 1.36 with $k = 0.9$ colored by the dig_T value for each orbit (right) and colored by the rotation number for regular orbits while black corresponds to chaotic orbits (left). These pictures were created by taking 1000 initial conditions each having an orbit length of 2000.

next section, we use the WBA to study chaos and quasi-periodicity for different billiard systems.

Results

We use the Chirikov standard map as a test case since, like the billiards map, it is a symplectic map with both chaotic and regular orbits. The Chirikov standard map is defined as follows:

$$\begin{aligned} \hat{x} &= x + \hat{y} \mod 1 \\ \hat{y} &= y - \frac{k}{2\pi} \sin(2\pi x). \end{aligned} \tag{1.36}$$

Figure 1.9 shows the phase space for the standard map with $k = 0.9$ and the color of each orbit represents the associated dig_T value from equation (1.35) for the orbit. Meiss and Sander in [42] found that a cut-off value of $\text{dig}_T = 5.5$ was sufficient for distinguishing an orbit as chaotic. We average the difference of the successive x coordinates for equation (1.36) by taking the difference $x_{k+1} - x_k$.

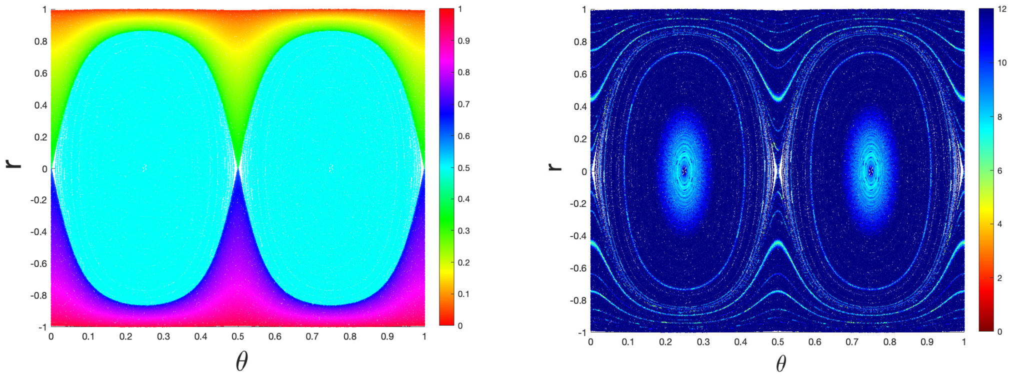

Figure 1.10: The phase space for the ellipse with $a_1 = 2$ and $b_1 = 1$ colored by rotation number (left) and dig_T value (right). The picture was created by taking 600 initial r values starting from 2 θ values, $\theta = 0.25, 0.5$. Unlike previous pictures, the white here are gaps in the initial conditions.

As another test case, we use the ellipse. We have already shown in figure 1.5 and again in figure 1.10, the phase space for the ellipse colored by rotation number. One can see that the rotation number is close to 1 on the upper and lower bounds of r indicating the ball is bouncing a very small amount each iteration. The dig_T value for this map as seen in figure 1.10 is the max value of dig_T, confirming that we have only non-chaotic orbits in the ellipse. We note that the equation for the rotation number for the rotational tori using definition 1.6.3 can be written as a Birkhoff average. Using θ from definition 1.2.3, we take $h(\theta_i) = f(\theta_i) - \theta_i$ and use this as our function h in equation (1.34). h therefore calculates the average amount of the circle traversed with each bounce. Das and Meiss used the same approach in [43].

Finally, we applied the WBA method to the case of the perturbed ellipse. Figure 1.11 shows the phase space for the billiard map on the perturbed ellipse where each orbit is colored by the dig_T value calculated for the orbit. We use equation (1.10) and take $a_1 = 1.1$, $a_2 = 0.03\epsilon$, $b_1 = 1$, and $b_2 = 0.025\epsilon$ where ϵ is varied between 0.1 and 1. Now when we perturb the ellipse we introduce a chaotic region, therefore a bimodal distribution arises separating those orbits that are chaotic from those that are non-chaotic. Figure 1.12 is a histogram of the dig_T values calculated for 1200 orbits each with length 2000 and length

10^4. We can see that there is a bimodal distribution in this histogram with the separation occurring between 4 and 5 for orbit length 2000 but this separation becomes more clear when the orbit length is 10^4. Calculating the WBA for orbits in multiple different perturbed ellipses, we found we found that a cut off value of $\text{dig}_T = 4.875$ was a sufficient value for distinguishing chaotic orbits from non-chaotic orbits when the orbit length is 2000. This cut off mostly agrees with larger orbit lengths as well. Treating the dig_T values calculated with orbit length 10^4 as truth, out of the 1200 orbits used to make the histograms, we found that there were 135 falsely labelled as chaotic and 160 falsely labelled as non-chaotic when the orbit length was $T = 2000$. It is worth noting that Newton's method for our method was set to have a tolerance of 10^{-14} so any values beyond that can be taken to be as having only 14 digits of accuracy.

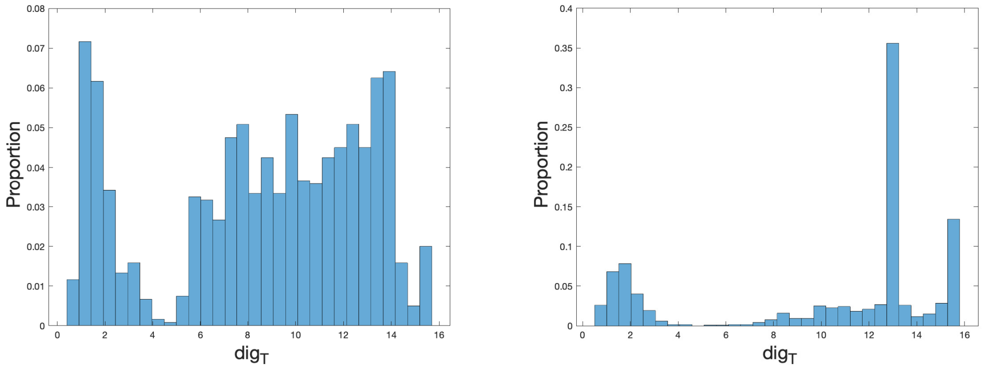

Figure 1.12: A histogram displaying the bimodal distribution obtained from calculating the dig values for 1200 orbits each with length 2000 (right) and length 10000 (left) in the perturbed ellipse.

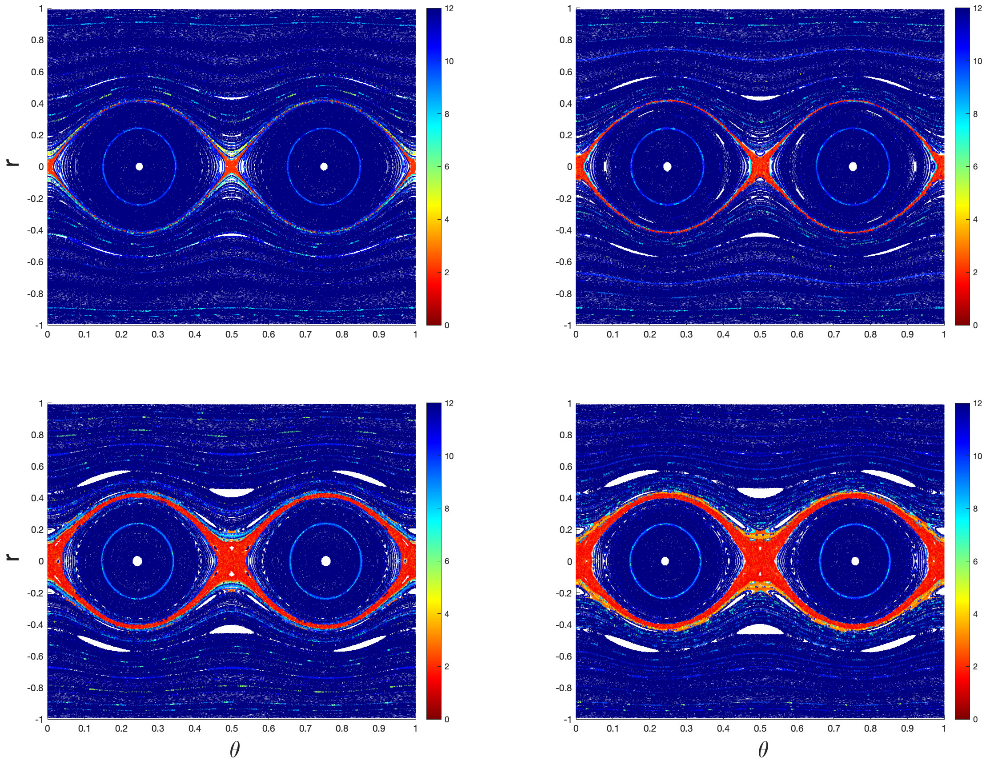

Figure 1.11: Phase Space for the billiard map on the perturbed ellipse given by equation (1.10) with coefficients $a_1 = 1.1$, $a_2 = 0.03\epsilon$, $b_1 = 1$, and $b_2 = 0.025\epsilon$ where ϵ is varied between 0.1 and 1. The color of each orbit represents the dig$_T$ value calculated for the orbit. Each picture was created by taking 1800 initial conditions across multiple different θ values. Each orbit has length 2000.

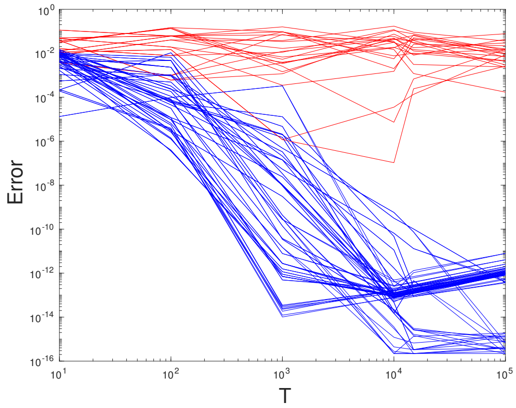

Figure 1.13: 100 initial trajectories were taken all starting from $\theta = 0.5$ for the perturbed ellipse with coefficients $a_1 = 1.1$, $a_2 = 0.03$, $b_1 = 1$, and $b_2 = 0.03$. The plot shows the convergence rate for the dig_T value of each orbit as we increase the number of points, T, in the orbit. The orbits in red are the chaotic orbits.

Figure 1.13 displays the convergence of these dig_T values calculated for 50 orbits starting from $\theta = 0.5$. We chose this initial θ value because the line of fixed θ intersects the chaotic sea (red part) with higher proportion. This figure is similar to Figure 2 produced by Meiss and Sander in [42]. They too found that 10^4 was an optimal orbit length for distinguishing chaotic orbits from non-chaotic orbits. In figure 1.13, we plot the length of the orbit T verses the WBA value calculated for that orbit. The chaotic orbits are colored in red while the regular orbits are colored blue. One can see that the chaotic orbits do not converge in the average as quickly as the non-chaotic orbits do. We can see from this figure that an orbit length of $T = 2000$ is mostly sufficient to determine whether an orbit is chaotic or regular in the billiard map, although for more accurate results an orbit length of $T = 10^4$ should be used since this is where complete separation of chaotic and non-chaotic occurs from the WBA perspective.

One issue that arises with our implicitly defined map is that our method always produces a θ value that is between 0 and 1 when solving equation (1.13). Thus, when the ball passes $\theta = 1$ in a counter-clockwise direction, the difference between the θ values would be negative when all previous iterates had a positive difference. Therefore, leading to issues in calculating the rotation number and subsequently the WBA for those orbits. For example, if the ball travels from $\theta = 0.6$ to $\hat{\theta} = 0.1$ (counter-clockwise rotation for the orbit), we would have a negative difference. Our solution to this issue was to find the difference between each consecutive contact point. If the difference was negative, we add one to the later θ value. This does not pose a problem when the balls path is in a clockwise rotation since the 1 would average out.

1.6.2 Periodic Orbits Using Multiple Shooting Method

In this section, we discuss a method for computing periodic orbits. We wish to find periodic orbits for billiards systems. We use the multiple shooting method, first proposed by Morrison et al. in [48]. Previously, this method has been used to find periodic orbits in maps on $\mathbb{R}^n$ [49]. However, we have added a way to deal with maps on the n-dimensional torus, $\mathbb{T}^n$. Given a function f, $\{p_1, p_2, ..., p_N\}$ is a periodic orbit under f if

$$f(p_j) = p_{j+1} \text{ for } j = 1, ..., N-1 \text{ and } f(p_N) = p_1. \tag{1.37}$$

One is tempted to apply Newton's method to $G(p) = f^N(p_k) - p_k$. However, this is less numerically stable than using the following system of equations. Let

$$P(x_1, ..., x_N) = \begin{bmatrix} f(x_N) - x_1 \\ f(x_1) - x_2 \\ \vdots \\ f(x_{N-1}) - x_N \end{bmatrix}.$$

Clearly, $\{p_1, ..., p_N\}$ is a period N orbit for f if and only if $P(p_1, ..., p_N) = 0$. Furthermore, f and P have the same smoothness properties. Since $f : \mathbb{R}^k \to \mathbb{R}^k$, and $P : \mathbb{R}^{Nk} \to \mathbb{R}^{Nk}$, $Df(\vec{x})$ is a $k \times k$ matrix and therefore $DP(\vec{x})$ is an $Nk \times Nk$ block diagonal matrix with

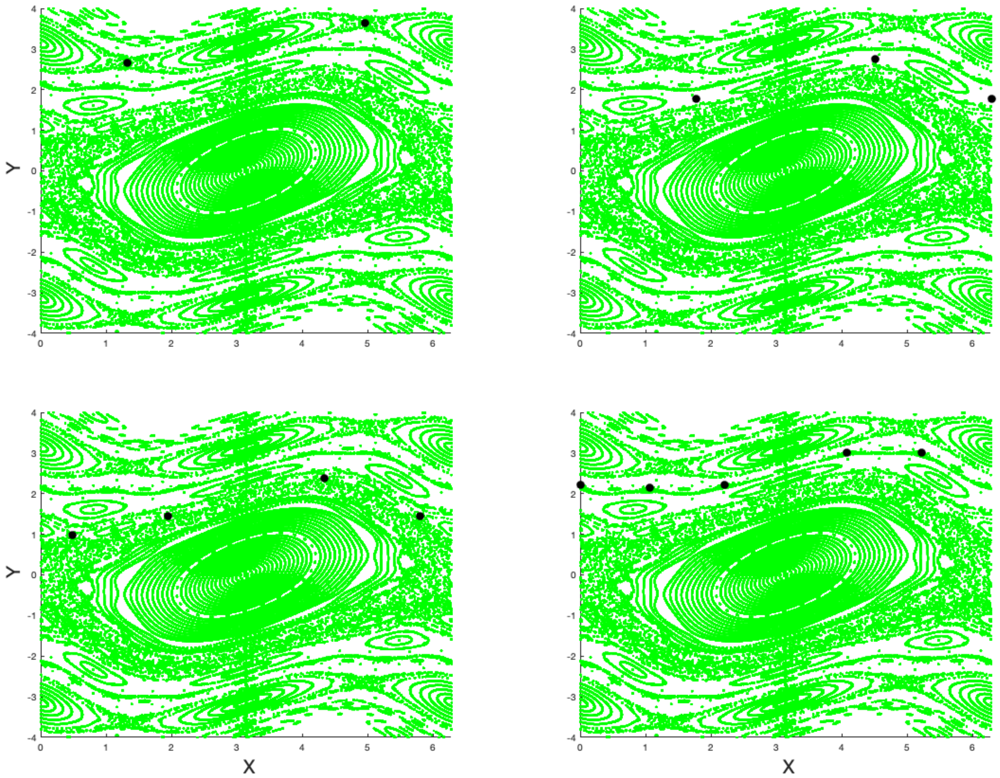

Figure 1.14: Applying the multiple shooting Newton's method to the standard map to find the two, three, four, and five period orbits, respectively, from top left to bottom right. The black dots represent the periodic orbit points.

the form

$$DP(\vec{x}) = \begin{pmatrix} -I & 0 & \cdots & Df(x_N) \\ Df(x_1) & -I & \cdots & 0 \\ \vdots & \ddots & \ddots & \vdots \\ 0 & \cdots & Df(x_{N-1}) & -I \end{pmatrix}$$

where I is the $k \times k$ identity matrix.

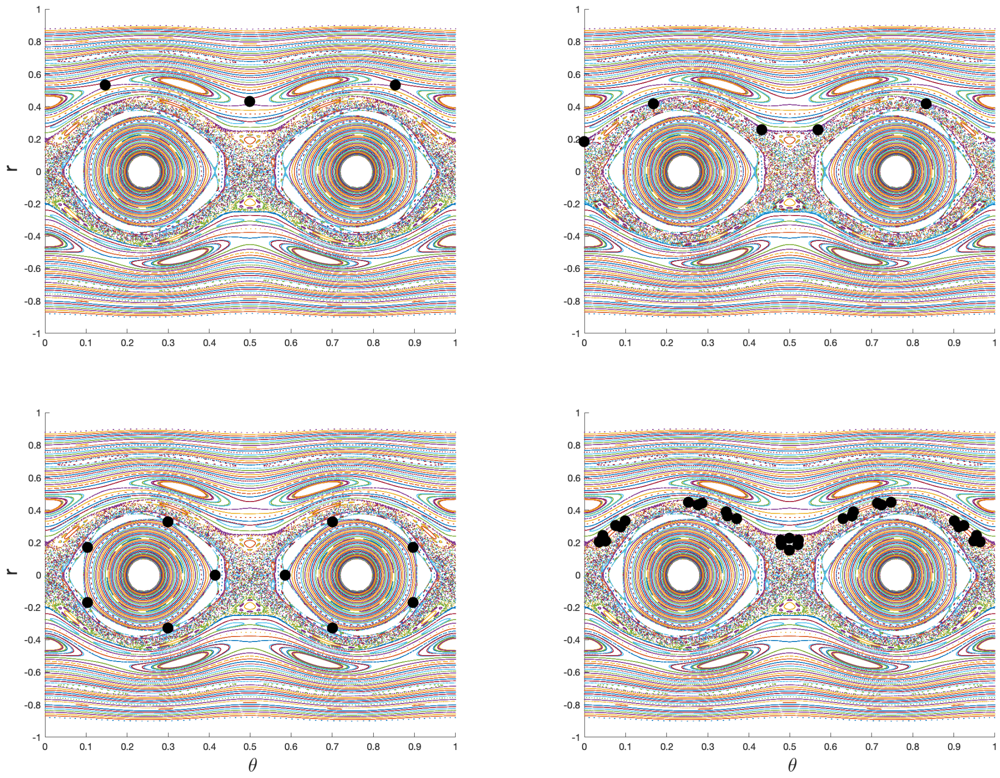

Figure 1.15: The phase space for the ellipse with the period 3, 5, 10, and 30 orbit denoted with large black circles.

Results

We start by using a test case of the Chirikov standard map as given by equation 1.36 to find the periodic orbits using the multiple shooting Newton's method. Figure 1.14 shows orbits of period 2, 3, 4, and 5 computed in this way.

We apply multiple shooting to the perturbed ellipse table to find several different periodic orbits. Figure 1.15 shows our computed period 3, 5, 10 and 30 orbits. Note that the period 10 orbit is contractible but the others are non-contractible.

1.7 Finding Manifolds with the Parametrization Method

In the following section, we will describe the parametrization method and how we will use it to calculate the stable and unstable manifold for maps on $\mathbb{T}^n$.

1.7.1 Parametrization Method

The parametrization method was first introduced by Cabré et al. in [50–52] to obtain a parametrization of the manifold that is adapted to its geometry, [53]. For an introduction and comprehensive discussion on the parametrization method, see [53]. In [49] and [54], this method was extended to discrete time dynamics. In [55], the parametrization method was used for implicitly defined maps but the functions were polynomials so the Taylor series could be found using convolutions. In this section we will give an overview of the parametrization method and show how we will apply this method to implicitly defined billiard maps (which are not defined by polynomials).

The parametrization method relies on two well known theorems in dynamical systems. From Robinson in [21], the Hartman-Grobman theorem for maps is as follows.

Theorem 1.7.1 (Hartman-Grobman Theorem)**.** *Let $f : \mathbb{R}^n \to \mathbb{R}^n$ be a C^r diffeomorphism with a hyperbolic fixed point p. Then there exists a neighborhood $U \subset \mathbb{R}^n$ of p and $V \subset \mathbb{R}^n$ of 0 and a homeomorphism $h : V \to U$ such that $f(h(x)) = h(Ax)$ for all $x \in V$, where $A = Df_p$.*

Let $\mathbb{E}^s$ denote the stable eigenspace which is spanned by the eigenvectors $\{\xi_k^s\}$ associated with the eigenvalues $\{\lambda_k^s\}$ each with $|\lambda_k^s| < 1$. Let $\mathbb{E}^u$ denote the unstable eigenspace which is spanned by the eigenvectors $\{\xi_k^u\}$ associated with the eigenvalues $\{\lambda_k^u\}$ each with $|\lambda_k^u| > 1$. We can define the local stable manifold for some neighborhood $U' \subset U$ of p as

$$W^s_{loc}(p, U') = \{x \in U' : f^n(x) \in U',\ \forall n \geq 0\}$$

and the global stable manifold as

$$W^s(p) = \bigcup_{j \geq 0} f^{-j}\left(W^s_{loc}(p)\right) = \{x \in \mathbb{R}^N : f^n(x) \to p \text{ as } n \to \infty\}.$$

The local unstable manifold for p in U' is defined as:

$$W^u_{loc}(p, U') = \{x \in U' : d(f^{-n}(x), p) \to 0\}$$

and the global unstable manifold as

$$W^u(p) = \bigcup_{j \geq 0} f^j \left(W^u_{loc}(p)\right) = \{x \in \mathbb{R}^N : f^{-n}(x) \to p \text{ as } n \to \infty\}.$$

Theorem 1.7.1 tells us that all orbits near the fixed point behave similarly to a linear map but the next theorem will give us more about these orbits behaviour near the fixed point. From Robinson in [21], the stable manifold for maps is stated as follows. Note that C^ω is the space of real analytic functions.

Theorem 1.7.2 (Stable Manifold Theorem)**.** *Let p be a hyperbolic fixed point for a C^k (C^ω) map $f : U \subset \mathbb{E} \to \mathbb{E}$ with $k \geq 1$. Then, there is some neighborhood of p, $U' \subset U$ such that $W^s(p, U', f)$ and $W^u(p, U', f)$ are each C^k (C^ω) embedded disks which are tangent to $\mathbb{E}^s$ and $\mathbb{E}^u$, respectively.*

Suppose f is a map with a hyperbolic equilibrium point $\hat{p}$. Assume that $Df(\hat{p})$ has eigenvalues such that none have modulus equal to 1, or $|\lambda| = 1$. Denote $k_s = \dim W^s$ and $k_u = \dim W^u$ where W^s, W^u are the stable and unstable manifold, respectively. Assume also that $Df(\hat{p})$ is diagonalizable, which implies we have a linearly independent set of eigenvectors and the number of eigenvectors equals the number of linearly independent eigenvalues. Denote the stable eigenvalues and corresponding eigenvectors by:

$$\left\{ \begin{array}{c} \lambda^s_1, \ldots, \lambda^s_{k_s} \\ \xi^s_1, \ldots, \xi^s_{k_s} \end{array} \right\}$$

and the unstable eigenvalues and eigenvectors by:

$$\left\{ \begin{array}{c} \lambda_1^u, ..., \lambda_{k_u}^u \\ \xi_1^u, ..., \xi_{k_u}^u \end{array} \right\}$$

where $|\lambda_1^s| < \cdots |\lambda_{k_s}^s|$ and $|\xi_1^s| < ... < |\xi_{k_s}^s|$. This also assumes the same ordering for the unstable eigenvalues as well. For this work, we will assume that our eigenvalues satisfy a non resonant condition meaning, no stable eigenvalue is a product of powers of the other stable eigenvalues.

Let $\hat{p} = (p_0, p_1, ..., p_{N-1})$ with $p_i \in \mathbb{R}^2$ denote a N periodic orbit under the map f such that $f^N(\hat{p}) = \hat{p}$. To find this periodic orbit, we employ the multiple shooting method outlined in section 1.6.2. We construct $F : \mathbb{R}^{2k} \to \mathbb{R}^{2k}$ such that

$$F(p_1, ..., p_{N-1}) = \begin{pmatrix} f(p_N) - p_1 \\ f(p_1) - p_2 \\ \vdots \\ f(p_{N-1}) - p_N \end{pmatrix}.$$

By proposition 3.1 in [49], λ is an eigenvalue of $DF(p)$ if and only if $\sqrt[n]{\lambda}$ is an eigenvalue of Df^N. After ordering the eigenvalues as above, we take the first eigenvalue of DF and perform the following.

We wish to find a smooth function $P : \mathbb{R}^{2k} \to \mathbb{R}^{2k}$ where k is either k_s or k_u that satisfies

$$P(0) = \hat{p} \quad \text{and} \quad \frac{\partial}{\partial \theta_j} P(\theta) = \xi_j$$

for all $1 \leq j \leq N$. We also wish for P to satisfy the conjugacy equation

$$f(P(\theta)) = P(\lambda\theta) \tag{1.38}$$

We know P exists by the stable manifold theorem and since P is smooth we can choose to write P in many different ways. We choose to find the Taylor series for P. As done in [49] and [54] we reformulate equation (1.38) for both the stable and unstable manifold to solve for P using Newton's method. We have

$$\begin{aligned} \Phi_s(\theta) &= P(\lambda\theta) - f(P(\theta)) \\ \Phi_u(\theta) &= P(\mu\theta) - f(P(\theta)) \end{aligned} \tag{1.39}$$

where $\mu = \frac{1}{\lambda}$. We use μ for the unstable case so that the power series can converge since $|\lambda^u| > 1$.

By theorem 1.7.1,

$$P(\theta) = \hat{p} + Df(\hat{p})\theta + \mathcal{O}(\theta^2)$$

so we know the 0th and 1st order terms for the Taylor expansion of P in equation (1.38) which are

$$P(\lambda\theta) = \hat{p} + Df(\hat{p})\lambda\theta + \mathcal{O}(\theta^2).$$

Now we need to find an expression for the right hand side of equation (1.38). We do this by finding the Fourier series for $f(P(\theta))$ using code written by Jason Mireles James and Jan Bouwe van den Berg. The series for each of the components of f is of the form

$$f_i(P(\theta)) = \sum b_j\theta^j$$

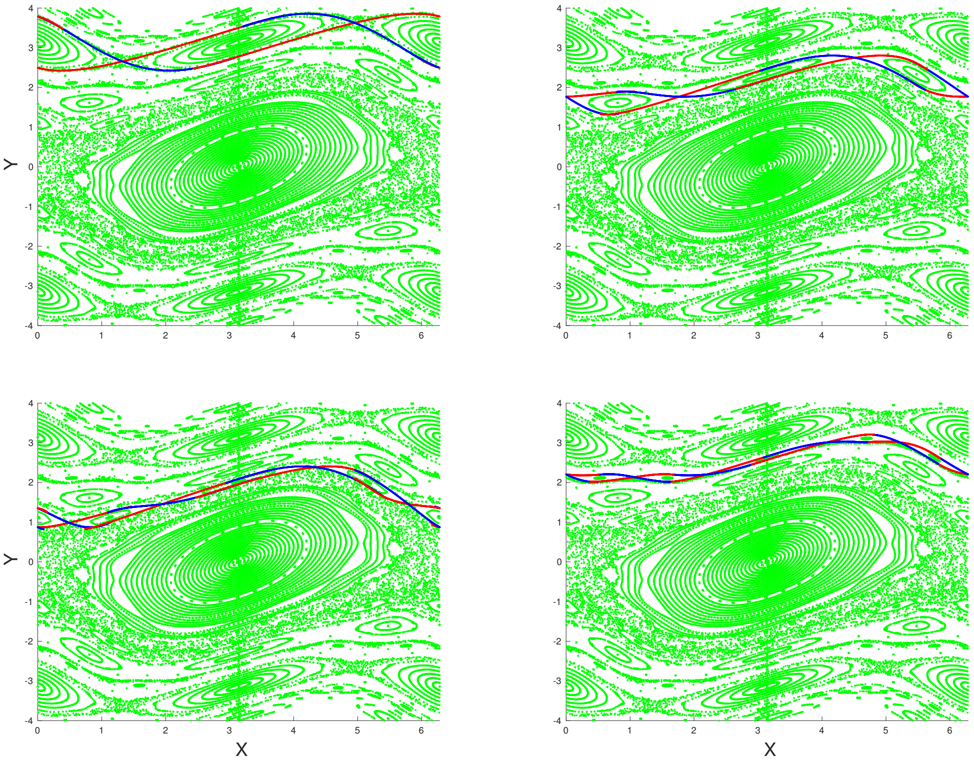

Figure 1.16: Stable (blue) and Unstable (red) manifolds calculated using the parametrization method for the 2, 3, 4, and 5 period orbits of the standard map.

for $i = 1, 2$. We can now write equation (1.39) as

$$\sum a_j \lambda^j \theta^j - \sum b_j \theta^j = 0.$$

Since the discrete Fourier coefficients are the coefficients for the Taylor series on the unit circle at the nth roots of unity, we can apply Newton's method to the difference of the coefficients to find a_j. We then repeat for each j.

Our results are as follows. As before with the multiple shooting method, we use the Chirikov standard map given by equation (1.36) as a test case for using the parametrization method on mod maps.

Figure 1.16 shows the approximation for the stable (red) and unstable (blue) manifolds for a period 2, 3, 4, and 5 orbit for the Chirikov standard map produced by the parametrization method outlined in the previous section.

1.8 Future Work

We have shown that the parametrization method can be successfully applied to maps on $\mathbb{T}^n$ by finding the stable and unstable manifolds in the Chirikov standard map. Our next goal is to calculate the stable and unstable manifolds for the implicitly defined billiard map on the perturbed ellipse. Afterwards, it would be worth looking into other implicitly defined maps such as delay differential equations outlined in the conclusion of [55].

Another goal we have for future work is to find a solution to $r = 0$. Other formulations for the implicit way we define our billiard map such as using the normal vector in the dot product instead of the tangent vector have produced the same issues while other formulations have shown promise to refine the issue down to a fewer number of cases. The next steps would be to verify the methods are analytic and implement them into our billiard map code.

Lastly, we need a way to make rigorously prove we have found the periodic orbit since we can only be sure of the orbit up to machine precision. The methods with interval arithmetic can be applied to give us a way to prove that we have accurately represented the periodic orbit, stable, and unstable manifolds which would typically be intractable to calculate by hand. Therefore we have set up our method in such a way that we would be able to use computer assisted proofs.

Chapter 2: Rate-Induced Break Up

2.1 Introduction

Recently, tipping points have been the subject of study for climate systems. There are three categories for tipping points: bifurcation tipping, noise induced tipping, and rate induced tipping. Most research has focused on dynamical systems containing some noise term, as in [56, 57]. Inspired by rate induced tipping, we discuss methods to detect coherent structure break up for deterministic equations with no attractor. Using the snapshot approach used by [58] and developed by [59], we look at a stroboscopic mapping of the periodically forced Duffing oscillator as the parameter is increased at a linear rate.

As an example, we will be focused on the periodically forced damped oscillator:

$$\ddot{x} = x - x^3 + p(t)\cos\omega t. \tag{2.1}$$

where $p(t)$ is a ramp function. In section 2.2, $p(t)$ will be constant. In section 2.3, $p(t)$ will be a linear ramp function but in section 2.4.2, we change $p(t)$ to a Heaviside function that linearly increases until a final value is reached, then remains constant. We perform a stroboscopic mapping by taking $t = \frac{2\pi k}{\omega}$ where $k \in \mathbb{N}$. When $p(t) = 0$, then every orbit is periodic. As $p(t)$ grows, more of these quasiperiodic orbits are destroyed and the area of chaos grows. In [58], a snapshot method is used to track the orbits proximity to the stable manifold of the snapshot hyperbolic point belonging to the time instant n_c, the time instant which signifies the iteration when the orbit starts to break up. Once an orbit has come sufficiently close to the stable manifold of the snapshot hyperbolic point, the snapshot tori become chaotic. See section 2.4.1 for a discussion on snapshot hyperbolic points. The conventional method for distinguishing chaos is by using Lyapunov exponents. A very useful method for detecting chaos has been the weighted Birkhoff average. In this chapter, we use a weighted Birkhoff average to help distinguish when snapshot tori break up into the chaotic sea and utilize these results to find criteria for rate induced break up of these coherent structures.

2.2 Periodically Forced Duffing Oscillator

We consider the periodically forced Duffing oscillator as presented in [58]:

$$\ddot{x} = x - x^3 + \epsilon \cos \omega t \tag{2.2}$$

and let $\epsilon = 0.01$ and $\omega = 1$. The system is Hamiltonian with Hamiltonian function:

$$H(x, y) = \frac{p^2}{2} - \frac{x^2}{2} + \frac{x^4}{4} - x\epsilon \cos \omega t.$$

As in [58], we take a stroboscopic mapping and consider the instants $t = \frac{2\pi k}{\omega}$, where k is a positive integer, thus we have a Poincaré section. See discussion below in 2.4.

Figure 2.1 was produced by taking $\epsilon = 0.01$ and following 2000 trajectories under (2.2). We solve the system by using ode45 in Matlab and setting a relative and absolute tolerance of 10^{-10}. A weighted Birkhoff average is applied to the first 1000 points in the trajectory and then the second 1000 points of the trajectory and then each trajectory is colored by its corresponding dig_T value. Instead of using the rotation number for our Birkhoff average as we did in the last chapter, we average the projection on the x axis for each orbit generated by the equation. We also used $h(x) = \cos 2\pi x$ as well but the dig_T values were about the same. We found that orbits with dig_T values less than 3 are chaotic and those with $\text{dig}_T > 3$ are non-chaotic.

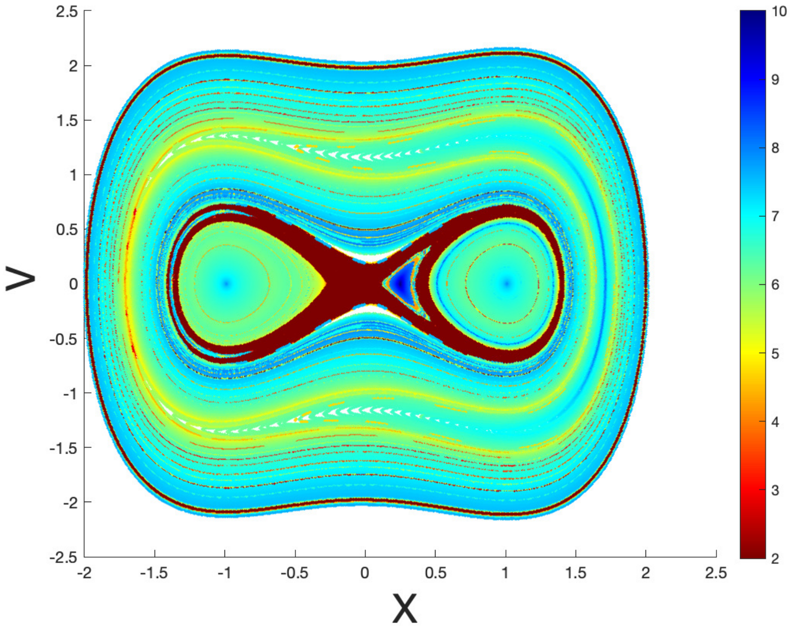

Figure 2.1: Periodically forced Duffing oscillator with $\epsilon = 0.01$. We set $\dot{v}(0) = 0, x(0) = 0$ to each of the 2000 points evenly spaced in $[-2, 2]$ and then follow each trajectory 2000 iterations. The color of each point represents the orbit's corresponding dig_T value.

2.3 Periodically Forced Duffing Oscillator with Parameter Drift

The next step was to apply the method to the forced Duffing oscillator with parameter drift. The system now being:

$$\ddot{x} = x - x^3 + p(t)\cos\omega t \tag{2.3}$$

where $p(t)$ is a ramp function. For this section we set $p(t) = \epsilon_0 + \alpha t$. with $\epsilon_0 = 0.01$, $\omega = 1$, and $\alpha = 0.001$.

We take a stroboscopic mapping by considering the time instances $t = \frac{2\pi k}{\omega}$, where $k \in \mathbb{Z}$. A stroboscopic map is a map that sets the value of the time variable at equal intervals. If p is periodic with period $\frac{2\pi}{\omega}$ then this would be a Poincaré section. The undrifted case would be an example of this. In the drifted case, we do not have a Poincaré section due to the parameter drift.

In [58], Jánosi and Tél used a stroboscopic mapping for the drifted Duffing oscillator. They used a similar approach to the snapshot attractors established by Romeiras et al. in [59] by looking at snapshot tori. Taking a KAM torus from the undrifted case, they evolve it under equation (2.3) for the flow. Jánosi and Tél declared an orbit to be chaotic when a point of the orbit intersects with the snapshot hyperbolic point's stable manifold which was accomplished by examining the average distance of point pairs on the ensemble of an initial torus. Once this distance grows exponentially, the subensemble begins exhibiting chaotic characteristics. A snapshot hyperbolic point being the equilibrium point with locally hyperbolic dynamics at each Poincaré section. We were able to replicate figure 4 in [58] by applying the method of weighted Birkhoff averages. This allowed us to find the break up of each torus without having to calculate Lyapunov exponents. After taking 100 points of x in $[-2, 2]$, we iterate under the equation (2.2) 2000 times. Then we take those points and iterate them under equation (2.3) to see how the parameter drift affects each torus. We started by applying the method of weighted Birkhoff averages to 5 orbits evenly distributed between $x = 0.18$ and $x = 0.2$ and letting $\dot{v}(0) = 0$. We iterated these 5 initial conditions for $N = 2000$ under equation (2.2) then used those points as initial conditions for equation (2.3) with $\alpha = 0.001$. Figure 2.2 depicts the tori snapshots for $n = 2, 4, 6$, and 8 with color representing the orbits corresponding dig_T value.

Figure 2.3 depicts the snapshots $n = 2$, 4, 6, and 8 for the larger phase space. We can see that as ϵ grows, the chaotic sea surrounding the two lobes grows as well. After $n = 40$, we see that the chaotic sea completely absorbs the left lobe of periodic orbits. Leaving only a U-shaped structure grouping of tori on the right hand side. Figure 2.4 depicts the histogram of dig_T values for 100 orbits taken between $x = -2$ and $x = 2$. We have picked a dig_T value of 3 as our cut off value since this is where the separation occurs for the bimodal distribution in the histograms. If an orbit has a dig_T value of less than 3, than it is chaotic. If the dig_T value is greater then 3, we label the orbit as quasi-periodic.

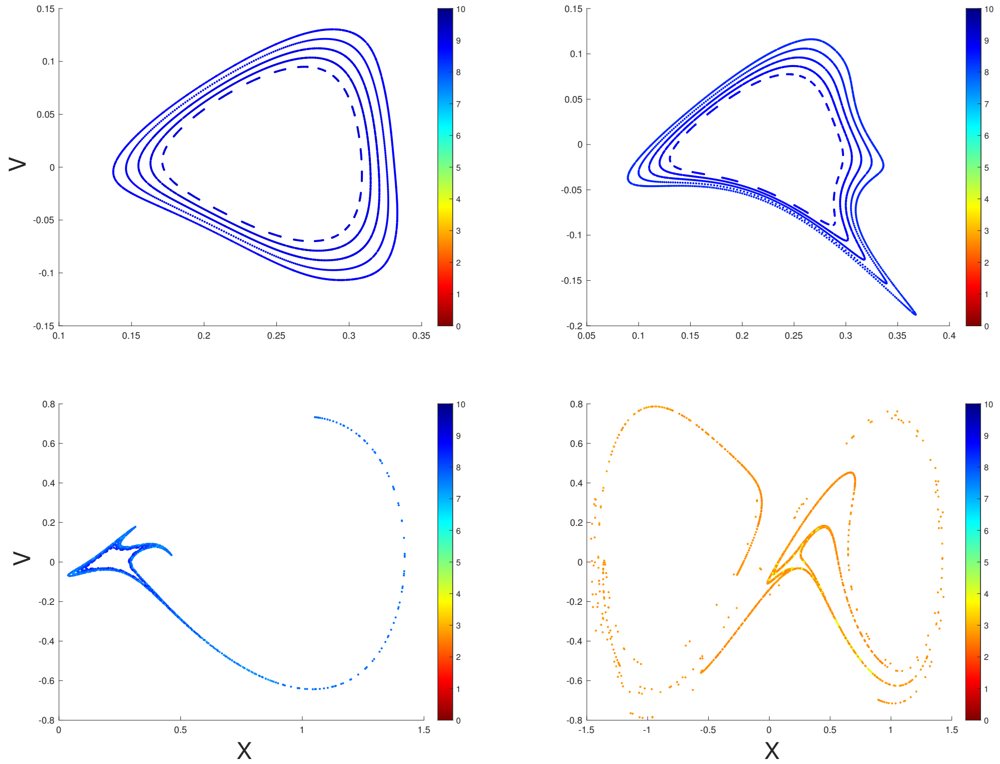

Figure 2.2: Evolution of tori captured at instants of $n = 2, 4, 6, 8$ for 5 initial conditions between $x(0) = 0.18$ and 0.2 with $v(0) = 0$ and $\alpha = 0.001$.

2.4 Rate Induced Tipping

One question that naturally arises from the previous section, is how does the value of α change the system. In other words, if one were to increase the rate of the ramp function, how would the system behave. This brings us to the topic of rate induced tipping.

2.4.1 Background on Rate Induced Tipping

Rate induced tipping has been a growing field in dynamics. Focus has been placed on dynamical systems with noise such as climate models. [60], sought to suggest appropriate definitions for rate induced tipping for asymptotically constant parameter shifts in terms of pullback attractors for non-autonomous systems. Suppose we have the non-autonomous

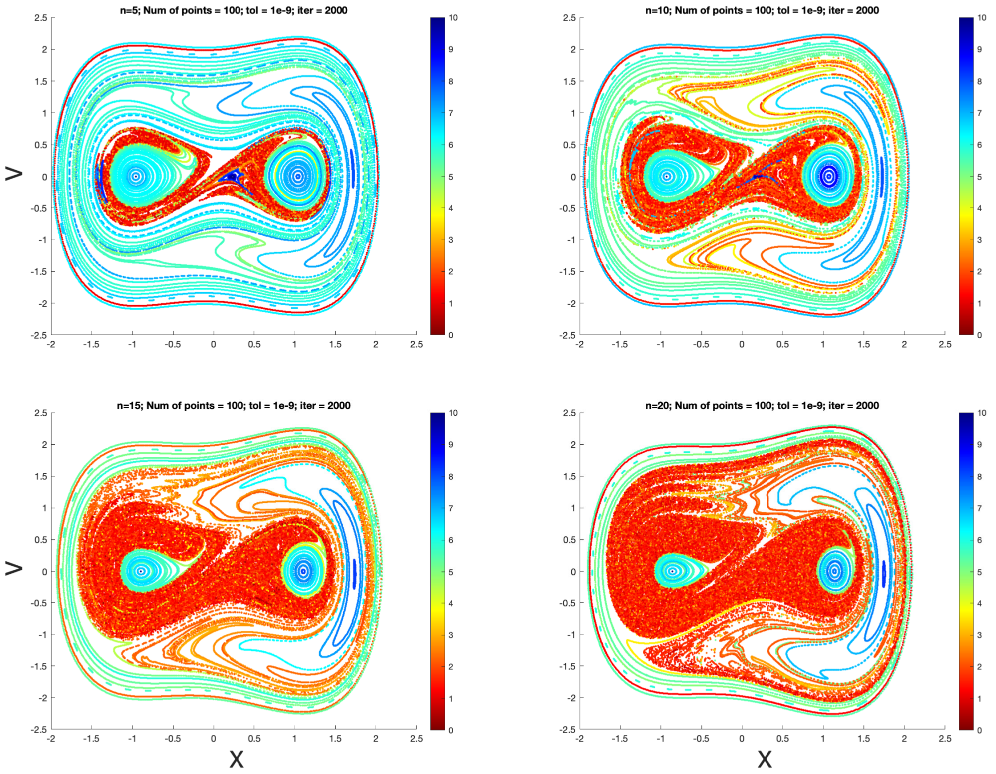

Figure 2.3: Drifted Duffing oscillator. Setting $v(0) = 0$ and taking 100 points between $[-2, 2]$ as $x(0)$. We set $\alpha = 0.001$ and $\epsilon_0 = 0.01$. Snapshot tori for n = 5, 10, 15, 20 (left to right; top to bottom). A tolerance of 10^{-8} was used.

system

$$\frac{dx}{dt} = f(x, p(rt)) \tag{2.4}$$

where $x \in \mathbb{R}^n$, and $p(t)$ is a time varying input. As in [60], we refer to the case that p is constant as the parametrized system with parameter p, and to its stable solution as the quasi-static attractor. Let

$$\mathcal{P}(p_-, p_+) = \left\{ p(t) : p_- < p(t) < p_+, \ \lim_{t\to\pm\infty} p(t) = p_\pm, \ \text{and} \ \lim_{t\to\pm\infty} \frac{dp}{dt} = 0 \right\}$$

and

$$X = \{(x, p) : f(x, p) = 0 \text{ and } p_- \leq p \leq p_+\}.$$

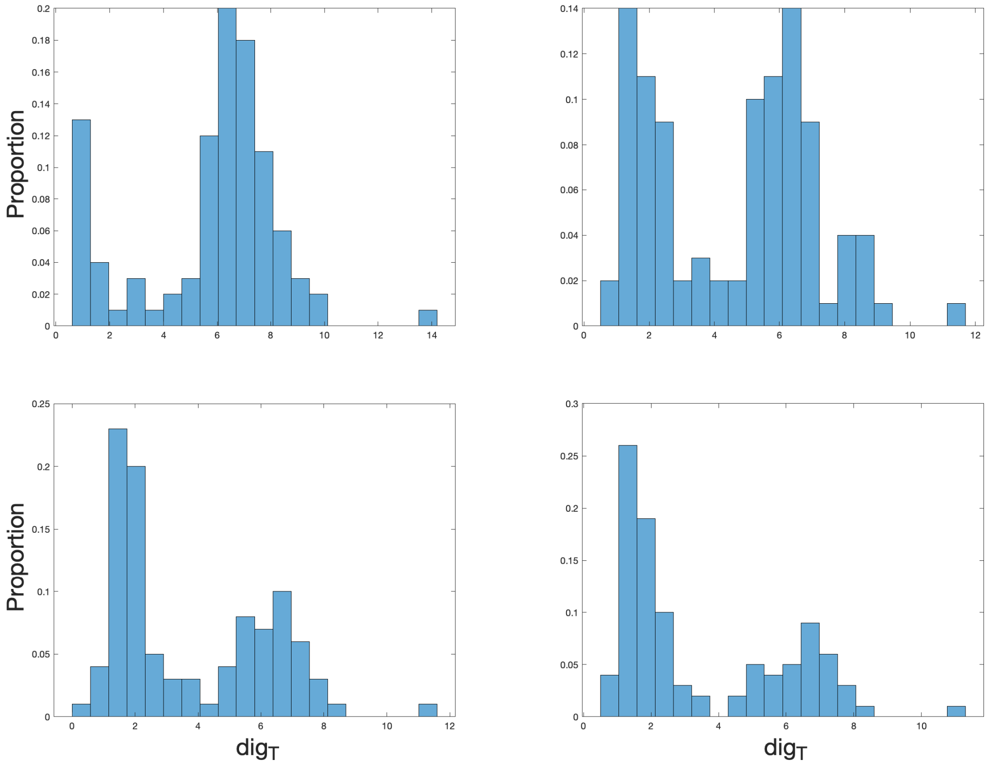

Figure 2.4: Histograms for the snapshot drifted Duffing oscillator at n = 5, 10, 15, 20. These are the corresponding histograms for the snapshot tori depicted in figure 2.3.

Therefore, we define the subset of X that is linearly stable as,

$$X_{stab} = \{(x, p) : \max\{\Re(\sigma(df(x, p)))\} < 0\}$$

where σ denotes the spectrum and $\Re$ denotes the real part of a value.

We will need a few preliminary definitions from [60] in order to formulate a criterion for rate-induced tipping. We first need to define some structure for our parameter drift.

Definition 2.4.1. *Given a parameter shift $p(t) \in \mathcal{P}(p_-, p_+)$, we say a continuous curve $(X(t), p(t))$ that limits to some $(X_\pm, p_\pm)$ as $t \to \pm\infty$ and whose image lies within X is a path. We say it is a stable path if its image lies within X_{stab}.*

Definition 2.4.2. *Consider a stable path* $(X(t), p(t))$ *from* (X_-, p_-) *to* (X_+, p_+)*. We say a solution* $x(t)$ *end-point tracks this path if it satisfies:*

$$\lim_{t \to \pm\infty} x(t) = X_\pm.$$

Definition 2.4.3. *Given a parameter shift* $p(t) \in \mathcal{P}(p_-, p_+)$*, we say points* (X_-, p_-) *and* (X_+, p_+) *on* X_{stab} *are* $p-$ *connected if they are the limiting points for some stable path* $(X(t), p(t))$*.*

Now that we have some proper definitions for our parameter drift, we can define rate-induced tipping as follows:

Definition 2.4.4. *Suppose that* $(X_-, p_-) \in X_{stab}$ *and fix* $p(t) \in \mathcal{P}(p_-, p_+)$*. We say there is irreversible rate induced tipping from* X_- *on* p *if there is a* $r_0 > 0$ *and a* X_+ *that is p-connected to* X_- *such that the system end-point tracks a stable path from* X_- *to* X_+ *for* $0 < r < r_0$ *but not for* $r = r_0$*.*

Ashwin et al. in [61], use similar definitions to define rate-induced tipping for linear systems. In [60], Ashwin et al. extend these methods to nonlinear systems by tracking trajectories under 2.4 with respect to a pullback attractor. They applied these definitions to model the evolution of global mean surface temperature. In [57], Ritchie and Sieber studied a prototypical model for rate-induced tipping, the saddle-node normal form subject to time-varying equilibrium drift and noise. They specifically were looking at how a system that is close to a rate-induced tipping event behaves under the influence of additive noise. In [62], Drótos et al study rate induced tipping on the Lorenz's atmospheric circulation model for midlatitudes on one hemisphere. They study this phenomenon by using snapshot attractors by evolving an ensemble of trajectories under the system until some final time. In [63], they prove that the occurrence of a rate-induced tipping coincides with the loss of uniform asymptotic stability by one of the locally pullback attracting solutions limiting at the stable equilibria of the past limit-problem. Ashwin et al. in [61], defined a tipping point as a sudden, large, and irreversible change in output of a complex system in response to a small change in input. They go on to define rate induced tipping to be when the system fails to track a continuously changing quasi-static attractor. This definition does not include equation (2.3) since we do not have an attractor. Thus, we cannot apply the methods used in [61], [60]. Therefore, for the case of the Duffing oscillator, we refer to the break up of coherent structures under different parameter drift rates as rate induced break up.

2.4.2 Rate of Alpha

We want to study whether rate induced tipping occurs with (2.3). Since equation (2.3) does not have an attractor, the previous discussion does not apply to this case. Inspired by rate induced tipping, we define rate induced break up as the break up of coherent structures due to a change of the rate of the parameter shift. Therefore we construct a ramping equation for p in the following way. Let

$$p(t,\alpha) = \begin{cases} \epsilon_0 + \alpha t, & t < \frac{\epsilon_f - \epsilon_0}{2\pi\alpha} \\ \epsilon_f, & t \geq \frac{\epsilon_f - \epsilon_0}{2\pi\alpha} \end{cases} \tag{2.5}$$

Keeping $\epsilon_0 = 0.01$ constant, we vary the parameter α to see if the system changes behaviour. For each α, we flow the points under equation (2.3) until we reach a final value $p(t) = \epsilon_f$. As an example, in Figure 2.6 we take 10 points in $x \in [1.6, 1.8]$ with $v = 0$. We flow these points under the Duffing oscillator. Then taking those coherent structures as initial conditions, we flow those trajectories under the drifted Duffing oscillator until we reach $n = 10$. For each picture in Figure 2.6 we have changed the value of α and evolved the system until we reach $\epsilon_f = 0.07$. For example, if $\alpha = 0.002$ then ϵ_f is reached at $n = 4$ snapshots. Thus, we evolve the system under the drifted Duffing oscillator until $n = 4$ then switch to ϵ_f for $n > 4$. In Figure 2.6, one can see as the value of alpha is increased, the U-shaped structure on the right lobe is stretched across the whole domain into a chaotic sea. As alpha increases, more and more of the U-shaped structure is absorbed into this chaotic band.

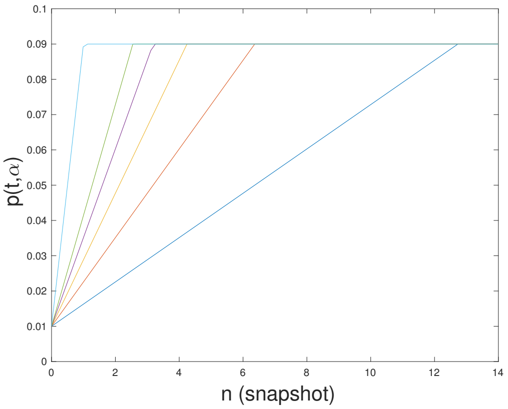

Figure 2.5: The picture displays the different ramps used to reach the final epsilon value. This particular case can be seen in the third row of table 2.1.

In table 2.1, we measure the percentage of chaotic trajectories in the system when the parameter drift reaches a specific value ϵ_f. Each column represents a different ramp α for p increased until ϵ_f is reached. Then the system is drifted until the final n snapshot. The final column represents instantaneous ramp used to reach each ϵ_f. It is clear the larger the ϵ_f value is the more chaotic orbits in the system. We conclude that with every row of the table, the faster the ramp, the more chaos is produced with the maximum being at the instantaneous ramp.

Table 2.1: Proportion of chaos as $p(t,\alpha)$ starts from $\epsilon_0 = 0.01$ and grows to ϵ_f then evolved until the final n value is reached. The value corresponding to the snapshot n is determined from equation (2.5). For reference, the amount of chaotic orbits in equation (2.2) is 15%.

Final n	ϵ_f	$\alpha = 0.001$	$\alpha = 0.002$	$\alpha = 0.003$	$\alpha = 0.004$	$\alpha = 0.005$	Instant
$n = 7$	$\epsilon_f = 0.05$	0.25	0.28	0.28	0.32	0.38	0.37
$n = 10$	$\epsilon_f = 0.07$	0.29	0.40	0.45	0.48	0.5	0.54
$n = 13$	$\epsilon_f = 0.09$	0.41	0.50	0.57	0.57	0.62	0.66
$n = 15$	$\epsilon_f = 0.1$	0.44	0.58	0.60	0.59	0.63	0.70

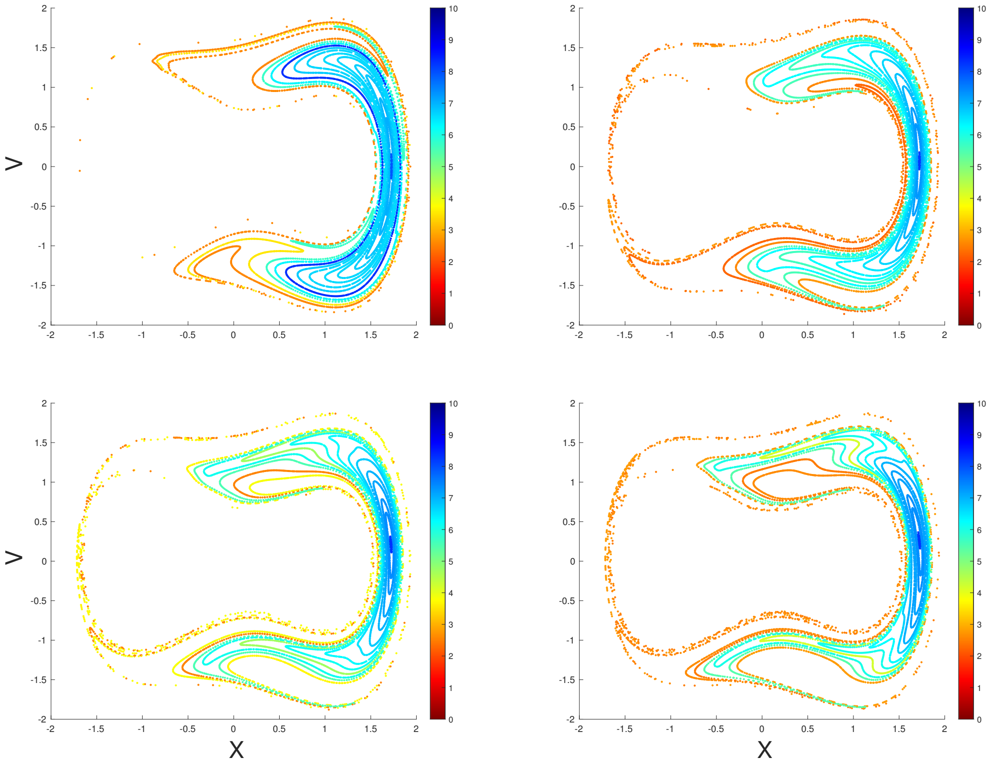

Figure 2.6: The trajectory of 10 points with $v(0) = 0$ and $x(0) \in [1.6, 1.8]$ drifted under different values of α until $\epsilon_f = 0.07$. From left to right and top to bottom: $\alpha = 0.001$, $\alpha = 0.002$, $\alpha = 0.003$, $\alpha = 0.004$.

The advantage of this method is that it only requires the orbit in order to find the break up of the tori. Previous methods relied on calculating the Lyapunov exponents or computation of the distances between points and an orbit. The WBA only requires the information from the orbit itself to test for when the tori break up. The WBA has been proven to be a faster way of distinguishing chaos than Lyapunov exponents.

2.5 Future Work

Future directions for rate induced break up are to further explore whether coherent structures, in the original undrifted Duffing equation, retain their structure under different parameter ramps. Fixing two values, ϵ_0 and ϵ_f, we would study the effects of different parameter ramps in terms of the invariant sets breaking up.

The detection of Lagrangian Coherent Structures (LCS) has been the focus of many fluid dynamics problems. The field of Lagrangian Coherent Structures (LCS) has been used to uncover special surfaces of trajectories that organize the rest of the flow into ordered patterns, [64]. The word Lagrangian in the LCS system conveys that the detected material surface must be evolving with the flow, [64]. In [65], they prove an analytic result that can be used to locate uniformly finite-time hyperbolic sets and their local stable and unstable manifolds in two dimensional time-dependent velocity fields. Their main theorem from this paper was applied to typical oceanic and atmospheric flows where the deformation rate of coherent structures is slower than typical particle speeds. In [66], they extend this two-dimensional analysis to three-dimensional velocity fields. In [64], Haller, focuses on deconstructing observed types of material coherence and then seeks the dynamical structures that create these forms of coherence in nonidealized flow data.

LCSs are typically categorized into two different groups: hyperbolic and elliptic LCS, [67]. In [67], they are able to detect elliptic LCSs by integrating the difference between two trajectories. The typical method used to detect hyperbolic Lagrangian structures is by using finite-time Lyapunov exponents (FTLE), [65]. There are a few issues that arise when using the FTLE approach that are outlined in [64]. In [68], Szezch et al show that one can use finite-time rotation numbers as a faster method for finding these structures. These methods lead me to believe that the method of weighted Birkhoff averages will be a useful tool for detecting these coherent structures as well as predict their breakup. An avenue of study for LCS is the comparison of WBA and FTLE systems like the two-dimensional model of the unsteady quadruple gyre flow outlined in [69] and the ABC flow map given in [65, 67].

Bibliography

[1] George Birkhoff. Dynamical systems. *Colloquium Publications*, Dec 1927.

[2] Artur Avila, Jacopo De Simoi, and Vadim Kaloshin. An integrable deformation of an ellipse of small eccentricity is an ellipse. *Annals of Mathematics*, 184(2):527558, Sep 2016.

[3] Amadeu Delshams and Rafael Ramírez-Ros. On birkhoff's conjecture about convex billiards. 10 1996.

[4] Vadim Kaloshin and Alfonso Sorrentino. On the integrability of birkhoff billiards. *Philosophical Transactions of the Royal Society A: Mathematical, Physical and Engineering Sciences*, 376(2131):20170419, Sep 2018.

[5] Luca Baracco and Olga Bernardi. Totally integrable symplectic billiards are ellipses. *Advances in Mathematics*, 454:109873, Oct 2024.

[6] Misha Bialy, Corentin Fierobe, Alexey Glutsyuk, Mark Levi, Alexander Plakhov, and Serge Tabachnikov. Open problems on billiards and geometric optics. *Arnold Mathematical Journal*, 8(34):411422, Jan 2022.

[7] L. A. Bunimovich. On ergodic properties of certain billiards. *Functional Analysis and Its Applications*, 8(3):254255, 1975.

[8] L. A. Bunimovich. On the ergodic properties of nowhere dispersing billiards. *Communications in Mathematical Physics*, 65(3):295312, Oct 1979.

[9] Nikolai Chernov and Roberto Markarian. *Chaotic billiards.* American Mathematical Society, 2006.

[10] George Datseris, Lukas Hupe, and Ragnar Fleischmann. Estimating lyapunov exponents in billiards. *Chaos: An Interdisciplinary Journal of Nonlinear Science*, 29(9), Sep 2019.

[11] L. A. Bunimovich. Physical versus mathematical billiards: From regular dynamics to chaos and back. *Chaos: An Interdisciplinary Journal of Nonlinear Science*, 29(9), Sep 2019.

[12] C.C. Bordeianu, D. Felea, C. Beliu, Al. Jipa, and I.V. Grossu. Chaotic dynamics in classical nuclear billiards. *Communications in Nonlinear Science and Numerical Simulation*, 16(1):324340, Jan 2011.

[13] Vivina L Barutello, Irene De Blasi, and Susanna Terracini. Chaotic dynamics in refraction galactic billiards. *Nonlinearity*, 36(8):42094246, Jun 2023.

[14] T Damour, M Henneaux, and H Nicolai. Cosmological billiards. *Classical and Quantum Gravity*, 20(9), Apr 2003.

[15] N. Berglund and H. Kunz. Integrability and ergodicity of classical billiards in a magnetic field. *Journal of Statistical Physics*, 83(12):81126, Apr 1996.

[16] Markus Himmelstrand and Victor Wilén. A survey of dynamical billiards. 2013.

[17] Mark Levi and Serge Tabachnikov. The poncelet grid and billiards in ellipses. *The American Mathematical Monthly*, 114(10):895908, 2007.

[18] J. D. Meiss. Symplectic maps, variational principles, and transport. *Reviews of Modern Physics*, 64(3):795848, Jul 1992.

[19] J. D. Meiss. *Differential Dynamical Systems.* Society for Industrial and Applied Mathematics, 2017.

[20] Christophe Golé. Symplectic twist maps. *Advanced Series in Nonlinear Dynamics*, 2001.

[21] Clark Robinson. *Dynamical systems: Stability, symbolic dynamics, and Chaos.* CRC Press, 2nd edition, 2009.

[22] Hillel Poritsky. The billard ball problem on a table with a convex boundary–an illustrative dynamical problem. *The Annals of Mathematics*, 51(2):446, Mar 1950.

[23] Vadim Kaloshin and Alfonso Sorrentino. On the local birkhoff conjecture for convex billiards. *Annals of Mathematics*, 188(1), Jul 2018.

[24] Misha Bialy and Andrey E. Mironov. The birkhoff-poritsky conjecture for centrally-symmetric billiard tables. *Annals of Mathematics*, 196(1), Jul 2022.

[25] Serge Tabachnikov. *Geometry and Billiards Serge Tabachnikov.* American Mathematical Soc, 2009.

[26] V F Lazutkin. The existence of caustics for a billiard problem in a convex domain. *Mathematics of the USSR-Izvestiya*, 7(1):185214, Feb 1973.

[27] John N. Mather and N. Mather. Glancing billiards. *Ergodic Theory and Dynamical Systems*, 2:397 – 403, 1982.

[28] Eugene Gutkin. Billiards in polygons. *Physica D: Nonlinear Phenomena*, 19(3):311333, Apr 1986.

[29] R. B. Carmo and T. Arajo Lima. Mixing property of symmetrical polygonal billiards. *Physical Review E*, 109(1), Jan 2024.

[30] Arseniy Akopyan, Richard Schwartz, and Serge Tabachnikov. Billiards in ellipses revisited. *European Journal of Mathematics*, 8(4):13131327, Sep 2020.

[31] Diogo Ricardo da Costa, Matheus Hansen, Mrio Roberto Silva, and Edson D. Leonel. Tangent method and some dynamical properties of an oval-like billiard. *International Journal of Bifurcation and Chaos*, 32(04), Mar 2022.

[32] Michael Turaev. *Numerical Experiments in Billiards*. PhD thesis, 2016.

[33] J. Solanpää, P.J.J. Luukko, and E. Rsnen. Bill2d a software package for classical two-dimensional hamiltonian systems. *Computer Physics Communications*, 199:133138, Feb 2016.

[34] Steven Lansel and Mason A. Porter. A graphical user interface to simulate classical billiard systems, May 2004.

[35] Eberhard Zeidler and Peter R. Wadsack. *Nonlinear functional analysis and its applications: I fixed-point theorems*. Springer, 1986.

[36] G. PETERS and J. H. WILKINSON. Practical problems arising in the solution of polynomial equations. *IMA Journal of Applied Mathematics*, 8(1):1635, 1971.

[37] Kenneth M. Brow and William B. Gearhart. Deflation techniques for the calculation of further solutions of a nonlinear system. *Numerische Mathematik*, 16(4):334342, Jan 1971.

[38] P. E. Farrell, Birkisson, and S. W. Funke. Deflation techniques for finding distinct solutions of nonlinear partial differential equations. *SIAM Journal on Scientific Computing*, 37(4), Jan 2015.

[39] Casper Beentjes. *Computing Bifurcation Diagrams with Deflation*. PhD thesis, 2015.

[40] Suddhasattwa Das, Chris B. Dock, Yoshitaka Saiki, Martin Salgado-Flores, Evelyn Sander, Jin Wu, and James A. Yorke. Measuring quasiperiodicity. *EPL (Europhysics Letters)*, 114(4):40005, 2016.

[41] Suddhasattwa Das and James A Yorke. Super convergence of ergodic averages for quasiperiodic orbits. *Nonlinearity*, 31(2):491501, 2018.

[42] E. Sander and J.D. Meiss. Birkhoff averages and rotational invariant circles for area-preserving maps. *Physica D: Nonlinear Phenomena*, 411:132569, October 2020.

[43] Suddhasattwa Das, Yoshitaka Saiki, Evelyn Sander, and James A Yorke. Quantitative quasiperiodicity. *Nonlinearity*, 30(11):41114140, 2017.

[44] Suddhasattwa Das, Yoshitaka Saiki, Evelyn Sander, and James A. Yorke. Solving the Babylonian problem of quasiperiodic rotation rates. *Discrete & Continuous Dynamical Systems - S*, 12(8):2279–2305, 2019.

[45] J.D. Meiss and E. Sander. Birkhoff averages and the breakdown of invariant tori in volume-preserving maps. *Physica D: Nonlinear Phenomena*, 428:133048, 2021.

[46] Nathan Duignan and James D. Meiss. Distinguishing between regular and chaotic orbits of flows by the weighted birkhoff average. *Physica D: Nonlinear Phenomena*, 449:133749, 2023.

[47] David Blessing and J.D. Mireles James. Weighted birkhoff averages and the parameterization method, Jun 2023.

[48] David D. Morrison, James D. Riley, and John F. Zancanaro. Multiple shooting method for two-point boundary value problems. *Communications of the ACM*, 5(12):613614, Dec 1962.

[49] J. L. Gonzalez and J. D. Mireles James. High-order parameterization of stable/unstable manifolds for long periodic orbits of maps. *SIAM Journal on Applied Dynamical Systems*, 16(3):17481795, Jan 2017.

[50] Xavier Cabré, Ernest Fontich, and Rafael de la Llave. The parameterization method for invariant manifolds i: Manifolds associated to non-resonant subspaces. *Indiana University Mathematics Journal*, 52(2):283328, 2003.

[51] Xavier Cabré, Ernest Fontich, and Rafael de la Llave. The parameterization method for invariant manifolds ii: Regularity with respect to parameters. *Indiana University Mathematics Journal*, 52(2):329360, 2003.

[52] Xavier Cabré, Ernest Fontich, and Rafael de la Llave. The parameterization method for invariant manifolds iii: Overview and applications. *Journal of Differential Equations*, 218(2):444515, Nov 2005.

[53] A. Haro, M. Canadell, J. Figueras, A. Luque, and J. Mondelo. *Parameterization method for invariant manifolds: From rigorous results to effective computations.* Springer, 2018.

[54] David Blessing and J. D. Mireles James. Weighted birkhoff averages and the parameterization method. *SIAM Journal on Applied Dynamical Systems*, 23(3):17661804, Jul 2024.

[55] Archana Neupane Timsina and J.D. Mireles James. Parameterized stable/unstable manifolds for periodic solutions of implicitly defined dynamical systems. *Chaos, Solitons & Fractals*, 161:112345, August 2022.

[56] Katherine Slyman and Christopher K. Jones. Rate and noise-induced tipping working in concert. *Chaos: An Interdisciplinary Journal of Nonlinear Science*, 33(1):013119, 2023.

[57] Paul Ritchie and Jan Sieber. Early-warning indicators for rate-induced tipping. *Chaos: An Interdisciplinary Journal of Nonlinear Science*, 26(9):093116, 2016.

[58] Dániel Jánosi and Tamás Tél. Chaos in Hamiltonian systems subjected to parameter drift. *Chaos: An Interdisciplinary Journal of Nonlinear Science*, 29(12):121105, December 2019.

[59] Filipe J. Romeiras, Celso Grebogi, and Edward Ott. Multifractal properties of snapshot attractors of random maps. *Physical Review A*, 41(2):784799, 1990.

[60] Peter Ashwin, Clare Perryman, and Sebastian Wieczorek. Parameter shifts for nonautonomous systems in low dimension: bifurcation- and rate-induced tipping. *Nonlinearity*, 30(6):2185–2210, June 2017.

[61] Peter Ashwin, Sebastian Wieczorek, Renato Vitolo, and Peter Cox. Tipping points in open systems: Bifurcation, noise-induced and rate-dependent examples in the climate system. *Philosophical Transactions of the Royal Society A: Mathematical, Physical and Engineering Sciences*, 370(1962):11661184, 2012.

[62] Gábor Drótos, Tamás Bódai, and Tamás Tél. Probabilistic concepts in a changing climate: A snapshot attractor picture. *Journal of Climate*, 28(8):32753288, 2015.

[63] Christian Kuehn and Iacopo P Longo. Estimating rate-induced tipping via asymptotic series and a melnikov-like method. *Nonlinearity*, 35(5):25592587, 2022.

[64] George Haller. Lagrangian coherent structures. *Annual Review of Fluid Mechanics*, 47(1):137162, 2015.

[65] G. Haller. Finding finite-time invariant manifolds in two-dimensional velocity fields. *Chaos: An Interdisciplinary Journal of Nonlinear Science*, 10(1):99108, 2000.

[66] G. Haller. Distinguished material surfaces and coherent structures in three-dimensional fluid flows. *Physica D: Nonlinear Phenomena*, 149(4):248277, 2001.

[67] Saviz Mowlavi, Mattia Serra, Enrico Maiorino, and L. Mahadevan. Detecting lagrangian coherent structures from sparse and noisy trajectory data. *Journal of Fluid Mechanics*, 948, 2022.

[68] J.D. Szezech, A.B. Schelin, I.L. Caldas, S.R. Lopes, P.J. Morrison, and R.L. Viana. Finite-time rotation number: A fast indicator for chaotic dynamical structures. *Physics Letters A*, 377(6):452456, 2013.

[69] Kristy L. Schlueter-Kuck and John O. Dabiri. Coherent structure colouring: Identification of coherent structures from sparse data using graph theory. *Journal of Fluid Mechanics*, 811:468486, 2016.

Biography

Patrick Bishop graduated in 2015 with a B.S in Mathematics with a concentration in applied mathematics from George Mason University. He began attending GMU graduate program in Fall of 2016 where he focused on dynamical systems, 3D printing mathematical objects and concepts including cylindrical anamorphisms, dual solids, and stable floating configurations for 2D objects.